mathematics

MDPI

Article

Exploring the Influence of Induced Magnetic Fields and Double-Diffusive Convection on Carreau Nanofluid Flow through Diverse Geometries: A Comparative Study Using Numerical and ANN Approaches

Shaik Jakeer [1], Seethi Reddy Reddisekhar Reddy [2], Sathishkumar Veerappampalayam Easwaramoorthy [3], Hayath Thameem Basha [4] and Jaehyuk Cho [3,*]

1 School of Technology, The Apollo University, Chittoor 517127, Andhra Pradesh, India; shaik_j@apollouniversity.edu.in
2 Department of Mathematics, Koneru Lakshmaiah Education Foundation, Bowrampet, Hyderabad 500043, Telangana, India; seethireddy@klh.edu.in
3 Department of Software Engineering, Jeonbuk National University, Jeonju-si 54896, Republic of Korea; sathish@jbnu.ac.kr
4 Department of Mathematical Sciences, Ulsan National Institute of Science and Technology, Ulsan 44919, Republic of Korea; basha666@unist.ac.kr
* Correspondence: chojh@jbnu.ac.kr

Abstract: This current investigation aims to explore the significance of induced magnetic fields and double-diffusive convection in the radiative flow of Carreau nanofluid through three distinct geometries. To simplify the fluid transport equations, appropriate self-similarity variables were employed, converting them into ordinary differential equations. These equations were subsequently solved using the Runge–Kutta–Fehlberg (RKF) method. Through graphical representations like graphs and tables, the study demonstrates how various dynamic factors influence the fluid's transport characteristics. Additionally, the artificial neural network (ANN) approach is considered an alternative method to handle fluid flow issues, significantly reducing processing time. In this study, a novel intelligent numerical computing approach was adopted, implementing a Levenberg–Marquardt algorithm-based MLP feed-forward back-propagation ANN. Data collection was conducted to evaluate, validate, and guide the artificial neural network model. Throughout all the investigated geometries, both velocity and induced magnetic profiles exhibit a declining trend for higher values of the magnetic parameter. An increase in the Dufour number corresponds to a rise in the nanofluid temperature. The concentration of nanofluid increases with higher values of the Soret number. Similarly, the nanofluid velocity increases with higher velocity slip parameter values, while the fluid temperature exhibits opposite behavior, decreasing with increasing velocity slip parameter values.

Keywords: Carreau nanofluid; induced magnetic field; wedge/plate/stagnation point; chemical reaction

MSC: 65N12; 76M22; 76M25; 80M25

check for updates

Citation: Jakeer, S.; Reddy, S.R.R.; Easwaramoorthy, S.V.; Basha, H.T.; Cho, J. Exploring the Influence of Induced Magnetic Fields and Double-Diffusive Convection on Carreau Nanofluid Flow through Diverse Geometries: A Comparative Study Using Numerical and ANN Approaches. *Mathematics* **2023**, *11*, 3687. https://doi.org/10.3390/math11173687

Academic Editors: José R. Fernánde and Lihua Wang

Received: 1 August 2023
Revised: 13 August 2023
Accepted: 25 August 2023
Published: 27 August 2023

1. Introduction

The circulation of blood is a fundamental component of human physiology, and comprehending its kinetics of paramount importance to numerous disciplines, such as biomedical engineering and healthcare investigation. The investigation of blood flow in bioengineering facilitates the development of medical equipment and innovations that can aid or supplant the operation of the cardiovascular system, including but not limited to artificial heart valves, stents, and pumps. Bioengineers can design devices that optimize blood flow, minimize turbulence, and reduce the risk of clotting by comprehending the fluid mechanics of blood flow. Additionally, these hemodynamic stresses can cause damage to blood vessels. The investigation of blood circulation is an essential aspect of medical research as it provides insights into various cardiovascular ailments and conditions, including but not limited to hypertension, atherosclerosis, and aneurysms. Medical professionals employ diverse methodologies, such as medical imaging and computational simulations, to scrutinize blood circulation in distinct areas of the circulatory system and evaluate the impact of different interventions or therapies. This knowledge facilitates physicians in the diagnosis and treatment of cardiovascular diseases with greater efficacy, and in the development of novel therapies that can enhance patient outcomes. The phenomenon of heat transfer holds significant importance in the context of blood circulation within the human body. The transportation of heat throughout the body is facilitated by blood, and the interaction between blood and the adjacent tissues in terms of heat exchange has an impact on various physiological mechanisms, including blood circulation [1–7]. Alghamdi et al. [8] examined the MHD flow of a hybrid nanofluid in a microcirculatory system with the use of the delivery procedure. The energy equation is purported to maintain a consistent temperature for the blood flow through the incorporation of the heat source/sink term. Dharmaiah et al. [9] investigated the features of heat transmission by examining the influence of the supply of blood velocity and circulation flow temperature slips via the Casson blood-flow ferromagnetic fluid throughout a sheet that was stretched through a wide range of fluid-controlling governing parameters. Jiang et al. [10] conducted research on a nonlinear fractional differential equation using the predictor-corrector compact difference system. Yang et al. [11] examine a space-time Sinc-collocation approach for solving the fourth-order nonlocal heat model emerging in viscoelasticity, a class of partial integrodifferential equations whose solution generally shows weak singularities at starting point time.

Artificial intelligence (AI), a branch of computer science, focuses on tasks with a defined goal, such as problem-solving, environmental adaption, decision-making, learning, and communication. Artificial intelligence (AI) finds application in diverse fields such as robotics, computer vision, pattern recognition, information retrieval, natural language processing, medical image computing, machine learning, image processing, data mining, knowledge representation, and other related domains. The artificial neural network (ANN) is a widely used methodology that emulates neural processes to mimic the cognitive functions of the human brain [12,13]. The significance of this factor is found to be crucial in addressing numerous intricate challenges in the field of physical engineering. Consequently, it is widely utilized with great efficacy in various mechanical systems such as combustion engines, refrigeration systems, and thermal devices. The researchers initially examined the effect of nanoparticle size, temperature, and particle concentration on thermal conductivity to estimate it using the ANN method. The utilization of artificial neural networks (ANN) is an effective method for the simulation of blood flow within the human circulatory system. This technique can facilitate the comprehension of the fundamental physiology and pathophysiology of diverse cardiovascular ailments. Artificial neural network (ANN) models have the potential to be trained on medical imaging data, including magnetic resonance imaging (MRI) or computed tomography (CT) scans. This can enable the prediction of blood flow patterns and the identification of areas within the circulatory system that may be compromised or obstructed. The aforementioned data have the potential to aid in the identification of cardiovascular ailments and strategizing of corresponding therapeutic interventions. Furthermore, artificial neural network (ANN) models have the potential to simulate the hemodynamics of blood flow within the circulatory system and investigate the impacts of different interventions or treatments. This methodology has the potential to facilitate researchers in comprehending the underlying mechanisms of diverse cardiovascular ailments and evaluating prospective therapeutic interventions. These models have been employed for the purpose of constructing predictive models for cardiovascular ailments, including hypertension, atherosclerosis, and aneurysms. Through the examination of extensive patient cohorts, researchers have the ability to instruct artificial neural network models to forecast the likelihood of disease development by utilizing diverse demographic, genetic, and environmental determinants [14–20]. Shilpa and Leela [21] explore the effects of local thermal nonequilibrium, induced magnetic field, and radiative heat on the magnetohydrodynamic mixed convective flow in the vertically circular permeable region. These effects are investigated using artificial neural networks (ANN) and LBM. The nanomaterial magnetohydrodynamic (MHD) flow of Ree–Eyring fluid between two spinning disks was analyzed utilizing an artificial neural network by Zhao et al. [22].

In the majority of scientific and practical applications for changing natural processes, viscoelastic non-Newtonian fluids are chosen over Newtonian fluids. The diverse properties of Newtonian materials cannot be adequately represented by a solitary constitutive relationship between sharing rate and stress (examples: water, air, alcohol and glycerol). The non-Newtonian paradigm encompasses a diverse array of constitutive relationships. Blood is classified as a non-Newtonian fluid due to its variable viscosity in response to changes in shear rate or applied force. At low shear rates, blood exhibits solid-like behavior, whereas at high shear rates, it exhibits liquid-like behavior [23–29]. The anomalous fluid dynamics exhibited by blood can be attributed to the existence of red blood cells, which possess the ability to undergo deformation and alter their morphology in reaction to the externally imposed shear stress. Under conditions of low shear rates, red blood cells have a tendency to aggregate and coalesce, resulting in the formation of clusters that contribute to an elevation in blood viscosity. Under conditions of high shear rates, the erythrocytes undergo alignment and directional flow, resulting in a reduction in blood viscosity. Comprehending the non-Newtonian characteristics of blood holds significant importance in numerous medical domains, including but not limited to blood rheology, hemodynamics, and blood flow simulations. The aforementioned phenomenon holds significant ramifications for the identification and management of cardiovascular ailments, including thrombosis, wherein alterations in blood viscosity can exert an impact on the genesis and endurance of blood coagulation. Comprehending the flow characteristics of biological fluids holds significance in the development of tissue-engineered structures that can emulate the performance of native tissues. Nanoparticles in an MHD Carreau fluid were subjected to a time-dependent stretching sheet with heat radiation and examined for their effects of multislip with multistratification by Faraz et al. [30]. Algehyne et al. [31] study the mixed convection flow of micropolar Carreau–Yasuda hybrid nanoliquid across a convectively heated Riga plate at a stagnation point. Shojaei et al. [32] used molecular dynamics simulation to study the impacts of atomic percentage and size of zinc nanoparticles as well as atomic porosity on the thermal behavior and mechanical performance of reinforced calcium phosphate cement. Koochaki et al. [33] employed the molecular dynamics technique and LAMMPS (www.lammps.org (accessed on 1 January 2023)) software to examine the atomic and mechanical performance of a polyethylene glycol-based hydrogel–cellulose nanocomposite as a wound-healing biostructure. Almitani et al. [34] investigated the impact of numerous surfactants on the thermal conductivity of nanofluids made of silica and deionized water. The nanofluids used in this investigation were produced using a two-step process.

Biomedical engineers, medical scientists, and physicians are interested in observing blood flow rate since it is used to diagnose cardiovascular disorders, including atherosclerosis and arrhythmia. Numerous researchers have investigated blood flow through the cardiovascular system using various non-Newtonian fluid models. Due to its shear-thinner characteristics, the Carreau fluid model may more precisely depict the rheological behavior of blood. Furthermore, magnetic properties are a noninvasive diagnostic tool that can be used to identify a variety of diseases and conditions, such as tumors, joint injuries, and injuries to the brain and spinal cord. The primary objective of the current study is to demonstrate the occurrence of double-diffusive convection in the radiative flow of blood nanofluid over three distinct geometries, namely plate, wedge, and stagnation point, under the influence of an induced magnetic field. The current literature has been extensively reviewed, revealing a lack of attempts to demonstrate the flow of forced convective blood nanofluid over three distinct geometries in the occurrence of an induced magnetic field. The current framework involves the utilization of Carreau nanofluid as a substitute for blood. The current issue is modeled using the nonhomogeneous equilibrium model. The current model has the potential to be utilized for the analysis of fluid transport characteristics in blood flow within a cardiovascular system, catheterized artery, and various hyperthermia treatments, such as cancer therapy. The self-similarity variables that were acquired are appropriate for accommodating any fluid Prandtl number. This study presents a new method for intelligent numerical computation, which involves the use of a Levenberg–Marquardt algorithm-based MLP feed-forward back-propagation ANN implementation [35,36]. The implementation of suitable self-similarity variables has enabled the transformation of equations governing fluid transport into equations of ordinary differential nature. The aforementioned equations were solved using the Runge–Kutta–Fehlberg (RKF) numerical integration technique.

2. Problem Formulation

The schematic illustration of three different geometries is shown in Figure 1. This study focuses on the Falkner–Skan unsteady forced convective flow of blood nanofluid. It is assumed that the velocity of the potential flow out from the boundary layer is given by the equation $u_\infty = b^{xm}$, with b standing for the constant. In the provided equations, u and v are the velocity components along the x and y directions. The wall's temperature (T_w) and concentration (C_w) are elevated compared to the ambient temperatures (T_∞) and concentrations (C_∞). It is assumed that a magnetic field of uniform induction with an intensity of $H_0 = H_e$ is applied to the surface in a direction perpendicular to it. Once H_2 reaches the surface and H_1 attains the value of H_0, the induced magnetic field's typical component vanishes.

- This study investigates the properties of forced convective flow of Cross nanofluid, which is characterized by its laminar, steady, and incompressible nature.
- The formula for momentum neglects the body force, such as the Lorentz force.
- The rheological behavior of blood nanofluid is characterized using the Carreau nanofluid model.
- Viscose dissipation and impacts from linear radiation are taken into account in the temperature equation. The Buongiorno nanofluid model is employed to simulate the governing equations.
- The mass transfer equation incorporates a chemical reaction of a destructive nature.
- $n = \frac{1}{6}$ for plate, wedge, and stagnation point of a flat plate.
- $m = \left(\frac{1}{(2/\beta_1)-1}\right)$ β_1 = 0, 0.5, 1 represents plate, wedge and stagnation point, respectively, $n_1 \in [0,1]$.

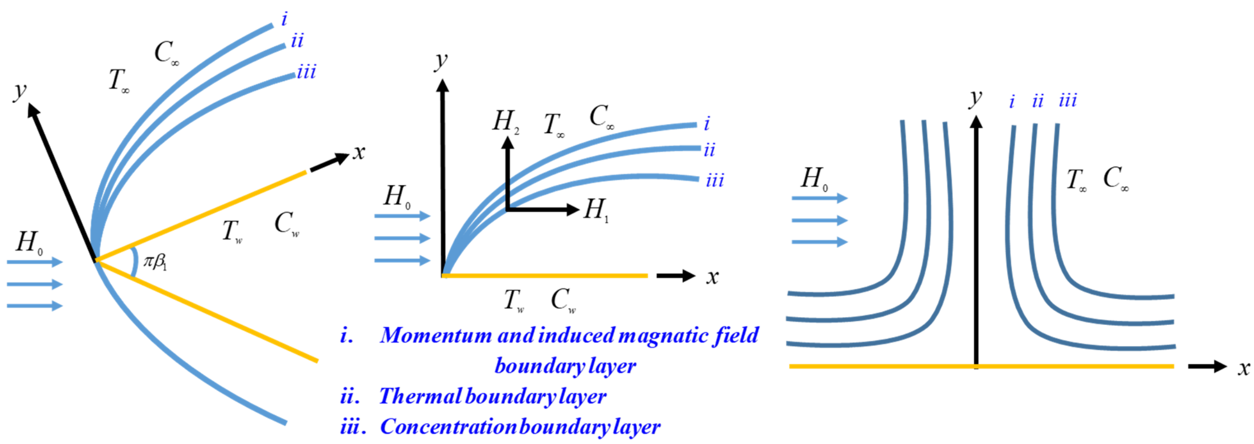

Figure 1. Geometrical description of the model.

The aforementioned factors have led to the expression of the fluid transport equations in Cartesian coordinates (x, y) for the current problem [37–41].

Continuity equation:

$$\frac{\partial u}{\partial x} + \frac{\partial v}{\partial y} = 0 \tag{1}$$

Momentum equation:

$$\begin{gathered} u\frac{\partial u}{\partial x} + v\frac{\partial u}{\partial y} = u_\infty \frac{du_\infty}{dx} - \frac{\mu_{mp} H_e}{4\pi\rho_f}\frac{dH_e}{dx} + \frac{\mu_{mp}}{4\pi\rho_f}\left(H_1\frac{\partial H_1}{\partial x} + H_2\frac{\partial H_1}{\partial y}\right) \\ +v_f\frac{\partial^2 u}{\partial y^2}\left[1+\Gamma^2\left(\frac{\partial u}{\partial y}\right)^2\right]^{\frac{n_k-1}{2}} + v_f(n_k-1)\Gamma^2\left(\frac{\partial u}{\partial y}\right)^2\frac{\partial^2 u}{\partial y^2}\left[1+\Gamma^2\left(\frac{\partial u}{\partial y}\right)^2\right]^{\frac{n_k-3}{2}} \end{gathered} \tag{2}$$

Induced magnetic field equation:

$$u\frac{\partial H_1}{\partial x} + v\frac{\partial H_1}{\partial y} - \mu_e\frac{\partial^2 H_1}{\partial y^2} = H_1\frac{\partial u}{\partial x} + H_2\frac{\partial u}{\partial y} \tag{3}$$

Energy equation:

$$u\frac{\partial T}{\partial x} + v\frac{\partial T}{\partial y} = \alpha_f\frac{\partial^2 T}{\partial y^2} + \tau\left(D_B\frac{\partial T}{\partial y}\frac{\partial C}{\partial y} + \frac{D_T}{T_\infty}\left(\frac{\partial T}{\partial y}\right)^2\right) - \frac{1}{(\rho c_p)_f}\frac{\partial q_r}{\partial y} + \frac{D_m k_T}{c_{p_f} c_s}\frac{\partial^2 C}{\partial y^2} \tag{4}$$

Concentration equation:

$$u\frac{\partial C}{\partial x} + v\frac{\partial C}{\partial y} = D_B\frac{\partial^2 C}{\partial y^2} + \frac{D_T}{T_\infty}\frac{\partial^2 T}{\partial y^2} - K_r^2(C-C_\infty) + \frac{D_m k_T}{T_m}\frac{\partial^2 T}{\partial y^2} \tag{5}$$

Subject to the boundary conditions

$$\begin{gathered} u = L_1\frac{\partial u}{\partial y}\left[1+\Gamma^2\left(\frac{\partial u}{\partial y}\right)^2\right]^{\frac{n_k-1}{2}}, v=0,\ \frac{\partial H_1}{\partial y} = H_2 = 0,\ -k_f\frac{\partial T}{\partial y} = h_f(T_w - T), C = C_w\ at\ y=0, \\ u = u_\infty,\ H_1 = H_e \to H_0,\ T\to T_\infty,\ C\to C_\infty\ as\ y\to\infty. \end{gathered} \tag{6}$$

where $u_\infty = bx^m$ is the free stream velocity, b is the constant. The parameter $\lambda = \delta_1\sqrt{\mathrm{Re}}$, which is suitable to choose any fluid Prandtl number value. Here, $\delta_1 = \sqrt{\frac{\mathrm{Pr}}{(1+\mathrm{Pr})^{2n}}}$, $n = \frac{1}{6}$ for plate, wedge and stagnation point of a flat plate, and $\mathrm{Re} = \frac{x u_\infty}{v_f}$ is the Reynolds number.

The radiative heat flux is provided in Equation (4) by

$$q_r = -\frac{4\sigma^*}{3k_1^*}\frac{\partial T^4}{\partial y}, \tag{7}$$

where k_1^* is the mean absorption coefficient and σ^* is the Stefan–Boltzmann constant. If the temperature gradients within the blood flow mass are negligibly small, then Equation (7) can be linearized by expanding T^4 into the Taylor's series about T_∞, and neglecting higher-order terms, we obtain

$$T^4 \cong 4T_\infty^3 T - 3T_\infty^4 \tag{8}$$

The appropriate variables for self-similarity are formulated in the following approach [38].

$$\begin{aligned} &\eta = \lambda\left(\frac{y}{x}\right),\ f(\eta) = \frac{\psi(x,y)}{\lambda\alpha^*},\ u = \frac{bx^m f'(\eta)}{(1+\mathrm{Pr})^{2n}}, H_1 = \frac{H_0 g'(\eta) x^m}{(1+\mathrm{Pr})^{2n}}, \\ &v = -\lambda\left(\frac{\alpha_f}{x}\right)\left[\frac{m+1}{2}f(\eta) + \frac{m-1}{2}\eta f'(\eta)\right], \\ &H_2 = -\frac{H_0\lambda}{b}\left(\frac{\alpha_f}{x}\right)\left[\frac{m+1}{2}g(\eta) + \frac{m-1}{2}\eta g'(\eta)\right], \\ &T = T_\infty + (T_W - T_\infty)\theta(\eta), C = C_\infty + (C_W - C_\infty)\phi(\eta). \end{aligned} \tag{9}$$

Substituting Equation (9) into the Equations (2)–(6), we obtain

$$\begin{aligned}&\Pr\left(\tfrac{d^3}{d\eta^3}f(\eta)\right)\left(1+n_k\tfrac{\Pr We^2}{(1+\Pr)^{6n}}\left(\tfrac{d^2}{d\eta^2}f(\eta)\right)^2\right)\left[1+\tfrac{\Pr We^2}{(1+\Pr)^{6n}}\left(\tfrac{d^2}{d\eta^2}f(\eta)\right)^2\right]^{\frac{n_k-3}{2}}\\&-\beta_{mp}m(1+\Pr)^{4n}+m(1+\Pr)^{4n}-m\left(\tfrac{d}{d\eta}f(\eta)\right)^2+\left(\tfrac{m+1}{2}\right)f(\eta)\tfrac{d^2}{d\eta^2}f(\eta)\\&-\beta_{mp}\left(\tfrac{(m+1)}{2}g(\eta)\tfrac{d^2}{d\eta^2}g(\eta)-m\left(\tfrac{d}{d\eta}g(\eta)\right)^2\right)=0\end{aligned} \quad (10)$$

$$M_{mp}\Pr\frac{d^3}{d\eta^3}g(\eta)+\left(\frac{m+1}{2}\right)\left(f(\eta)\frac{d^2}{d\eta^2}g(\eta)-g(\eta)\left(\frac{d^2}{d\eta^2}f(\eta)\right)\right)=0 \quad (11)$$

$$\begin{aligned}&\left(1+\tfrac{4}{3}Rd\right)\tfrac{d^2}{d\eta^2}\theta(\eta)+\tfrac{(m+1)}{2}f(\eta)\tfrac{d}{d\eta}\theta(\eta)\\&+\Pr\left(N_T\left(\tfrac{d}{d\eta}\theta(\eta)\right)^2+N_B\tfrac{d}{d\eta}\theta(\eta)\tfrac{d}{d\eta}\phi(\eta)\right)+\Pr D_r\tfrac{d^2}{d\eta^2}\phi(\eta)=0\end{aligned} \quad (12)$$

$$\frac{\Pr}{Sc}\frac{d^2}{d\eta^2}\phi(\eta)+\frac{(m+1)}{2}f(\eta)\frac{d}{d\eta}\phi(\eta)+\frac{\Pr}{Sc}\frac{N_T}{N_B}\frac{d^2}{d\eta^2}\theta(\eta)-\gamma(1+\Pr)^{2n}\phi(\eta)+\Pr S_r\frac{d^2}{d\eta^2}\theta(\eta)=0 \quad (13)$$

Subject to the boundary conditions

$$\begin{aligned}&\tfrac{d}{d\eta}f(\eta)=\tfrac{\alpha_s\sqrt{\Pr}}{(1+\Pr)^n}\tfrac{d^2}{d\eta^2}f(\eta)\left[1+\tfrac{\Pr We^2}{(1+\Pr)^{6n}}\left(\tfrac{d^2}{d\eta^2}f(\eta)\right)^2\right]^{\frac{n_k-1}{2}},f(\eta)=0,\\&\tfrac{d^2}{d\eta^2}g(\eta)=g(\eta)=0,\ \tfrac{d}{d\eta}\theta(\eta)=-\tfrac{B_i(1+\Pr)^n}{\sqrt{\Pr}}(1-\theta(\eta)),\phi(\eta)=1\ at\ \eta=0\\&\tfrac{d}{d\eta}f(\eta)=\tfrac{d}{d\eta}g(\eta)=(1+\Pr)^{2n},\ \theta(\eta)\to0,\ \phi(\eta)\to0\ as\ \eta\to\infty\end{aligned} \quad (14)$$

where m is the Hartree pressure gradient parameter, $\Pr=\frac{v_f}{\alpha_f}$ is the Prandtl number, $We=\sqrt{\frac{\Gamma^2u_\infty^3}{xv_f}}$ is the Weissenberg number, $M_{mp}=\frac{\mu_e}{v_f}$ is the magnetic Prandtl number, $\beta_{mp}=\frac{\mu_{mp}}{4\pi\rho_f}\left(\frac{H_0}{b}\right)^2$ is the magnetic parameter, $N_T=\frac{\tau D_T(T_w-T_\infty)}{T_\infty v_f}$ is the thermophoresis parameter, $N_B=\frac{\tau D_B(C_w-C_\infty)}{v_f}$ is the Brownian motion parameter, $Rd=\frac{4\sigma^*T_\infty^3}{k_1{}^*k_f}$ is the radiation parameter, $S_r=\frac{D_mk_T(T_w-T_\infty)}{v_f(C_w-C_\infty)T_m}$ is the Soret number, $D_r=\frac{D_mk_T(C_w-C_\infty)}{v_f(T_w-T_\infty)c_{p_f}c_s}$ is the Dufour number, $Sc=\frac{v_f}{D_B}$ is the Schmidt number, $\gamma=\frac{xK_r^2}{u_\infty}$ is the chemical reaction parameter, $B_i=\frac{h_f}{k_f}\sqrt{\frac{xv_f}{u_\infty}}$ is the Biot number, and $\alpha_s=L_1\sqrt{\frac{u_\infty}{xv_f}}$ is the velocity slip parameter.

The values for the skin friction factor, heat transfer rate, and mass transfer rate are provided as follows:

$$\begin{aligned}&C_f^*=\tfrac{2\sqrt{\Pr}}{(1+\Pr)^{3n}}\left(1+\tfrac{\Pr We^2}{(1+\Pr)^{6n}}(f''(0))^2\right)^{\frac{n_k-1}{2}}f''(0),\\&Nu^*=-\left[1+\tfrac{4}{3}Rd\right]\theta'(0),\\&Sh^*=-\phi'(0).\end{aligned} \quad (15)$$

where $C_f^*=C_f\mathrm{Re}^{1/2}$, $Nu^*=Nu\mathrm{Re}^{1/2}\delta_1{}^{-1}$, $Sh^*=Sh\mathrm{Re}^{1/2}\delta_1{}^{-1}$, $Nn^*=Nn\mathrm{Re}^{1/2}\delta_1{}^{-1}$.

3. ANN Modeling

The artificial neural network is a contemporary computer system approach that is based on the concept of the human brain functioning as a network of interconnected neural cells. This phenomenon has been identified as a replication of the evolutionary process of neural networks observed in the human brain. This model exhibits comparable performance to the human brain with respect to optimization, clustering, learning, classification, prediction, and generalization [12].

The subsequent phrases outline the principal benefits of utilizing the artificial neural network methodology.

- The artificial neural network (ANN) has demonstrated remarkable effectiveness and efficacy even when deployed on a limited hardware infrastructure.
- The intricate process of class-distributed mapping is surprisingly simplified by the use of artificial neural networks.
- The input vector is responsible for determining the appropriate outcomes within the training set.
- The weights that represent outcomes are acquired through iterative training.

The artificial neural network (ANN) utilized in this study is a computational approach inspired by the human brain's network of interconnected neurons. It is designed to handle complex tasks such as problem-solving, learning, and prediction. The ANN consists of multiple layers, including an input layer that receives data, hidden layers that process information, and an output layer that generates predictions. The ANN model employed in this research is a multilayer perceptron (MLP) feed-forward network, which is a widely used architecture. It comprises nodes arranged in layers, with connections between nodes in adjacent layers. The back-propagation algorithm is utilized for training, which is applied to adjust the weights of connections iteratively to minimize prediction errors. A key parameter is the number of hidden layers and nodes, which is determined through iterative optimization. This ANN model is trained on data, utilizing 70% for training, 15% for validation, and 15% for testing. The model's ability to predict fluid flow characteristics, such as skin friction and heat transfer rates, is demonstrated through comparison with numerical simulations. The ANN's ability to capture intricate relationships within the data enables it to produce accurate predictions, offering an efficient alternative to traditional computational methods. The development of a training algorithm and the establishment of interneuronal connections yield diverse neural network structures. The stratification of neural networks is frequently attributed to the close interplay among individual neurons. The artificial neural network (ANN) methodology comprises three unique strata, namely the input, hidden, and output layers. The layers of the system receive external information, undergo processing, and subsequently transmit the output through the artificial neural network. The input layer transmits information to the hidden layer neurons in an unmodified state without undergoing any processing by the input layer's processing components. It is imperative to acknowledge that the weights, connection lines, and interconnecting neurons facilitate the transmission of information. A database is maintained by the system to facilitate training of artificial neural networks (ANNs), wherein input values and weights are stored. The construction of an artificial neural network is guided by the utilization of data, which takes into account various factors, such as determining the optimal number of layers and hidden neurons.

The multilayer perceptron architecture-based feed-forward neural network (FFNN) has gained significant popularity and interest as an artificial neural network (ANN) model and is currently the most commonly employed. Alternative techniques for training feed-forward neural networks exhibit inferior efficiency compared to the back-propagation method. The back-propagation algorithm is capable of modifying the weights of individual neurons during the computation of the network's output error. This weight adjustment is uniformly implemented across all neurons to reduce the output error.

The subsequent expression represents the net input of the jth hidden neuron, as depicted in Figure 2.

The ith node input layer is denoted as x_i, the jth node hidden layer is indicated as a_j, and the linking weight between x_i and a_j is represented as $W1_{ji}$.

The output's jth hidden node is represented as follows:

$$z_j(x) = \frac{1}{1 + e^{-y_j(x)}},$$

The output layer's kth node is indicated as follows:

$$o_k(x) = \sum_{j=1}^{m} W2_{kj} z_j + b_k$$

$W2_{kj}$ is the connecting weight between the kth node of the output layer and the jth node of the hidden layer, where b_k is the biasing term at the kth node of the output layer.

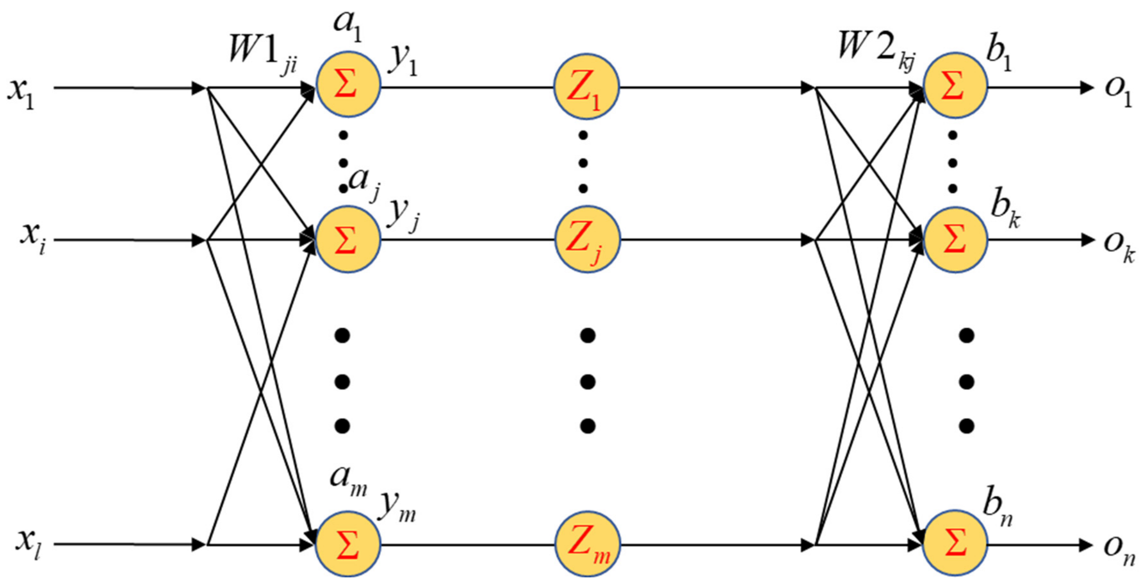

Figure 2. Schematic diagram of back-propagation in a neural network.

The present study involves the quantification of skin friction and heat transfer rates for representative samples of artificial neural network (ANN) output nodes, as depicted in Figure 3. The trained network's characteristics, including its layer counts, are listed in Table 1. The parameters We, β_{mp} and α_s and B_i, N_T, N_B, D_r, and S_r are estimated for the input node samples. The process of trial and error is employed to ascertain the optimal number of nodes in the hidden layer of a neural network, taking into account the number of training epochs necessary for the network, preventing the over- or under-setting of input parameters, and guaranteeing the successful completion of the learning process. After conducting multiple iterations, it was determined that the convergence criteria utilized involved the incorporation of a single hidden layer consisting of five neurons. This approach was implemented to mitigate the discrepancy between the projected values of C_f^*, Nu^*, and Sh^*. In the present study, 24 datasets are obtained for α_s, We, β_{mp}, and M_{mp}, and 48 datasets are obtained for α_s, We, β_{mp}, M_{mp}, Rd, N_T, N_B, D_r, S_r, γ, and B_i. It is important to note that the appropriate neural network can be chosen by minimizing the mean square error between the network model's target data and the sample data. The training process concludes upon reaching a point where the error stabilizes (see Figure 4), indicating that the trained network has achieved the desired level of accuracy. Figure 5 presents an error histogram showcasing errors detected during the training phase of the ANN. These values are small when considering the error values along the x-axis of this histogram. Upon examining the data histogram, which illustrates error values across three distinct data sets, it becomes apparent that the errors are heavily concentrated very close to the yellow line representing the zero-error threshold. These findings, derived from an analysis of the error histogram, conclusively demonstrate the successful completion of the ANN model's training phase, characterized by an impressively low error rate. The results pertaining to the skin friction coefficient and heat transfer rate in the training, validation, and test sets of the ANN model are presented in Figures 6 and 7. The provided elements equip artificial neural network models with the necessary components to replicate intricate relationships between input and output variables.

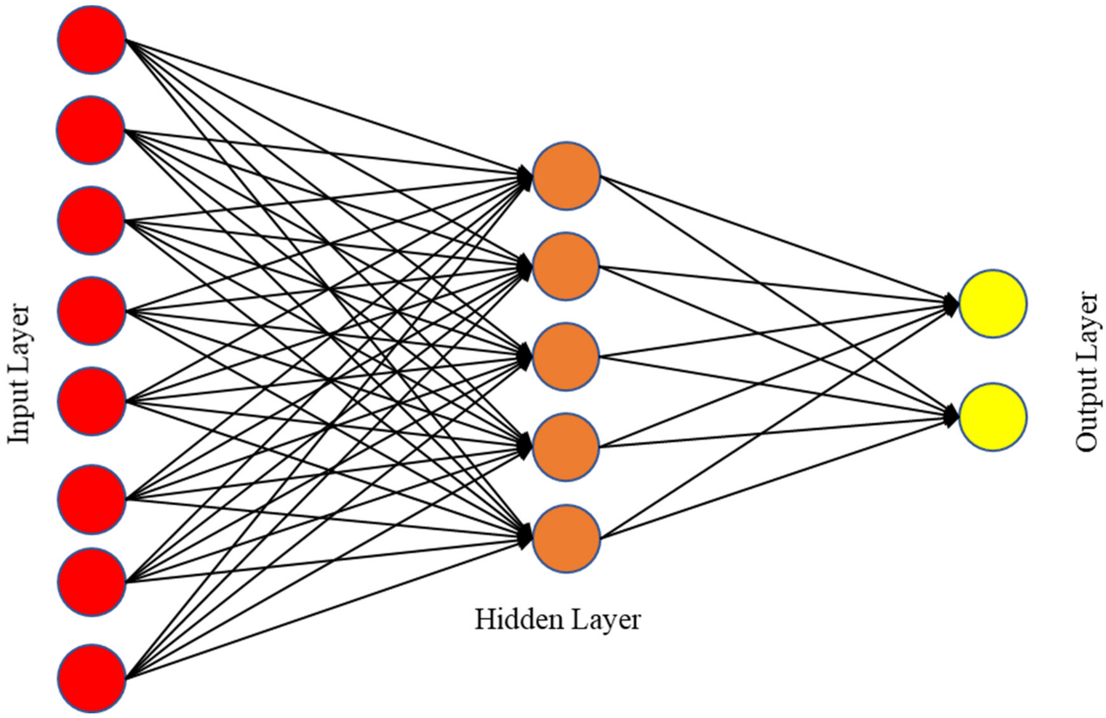

Figure 3. Schematic representation of a multilayer artificial neural network model.

Table 1. Neural networking detail.

Input Layer	Hidden Layers	Output Layer
4 (α_s, We, β_{mp}, and M_{mp})	3	1 (skin friction factor)
11 (α_s, We, β_{mp}, M_{mp}, Rd, N_T, N_B, D_r, S_r, B_i and γ)	5	2 (heat and mass transfer rate)

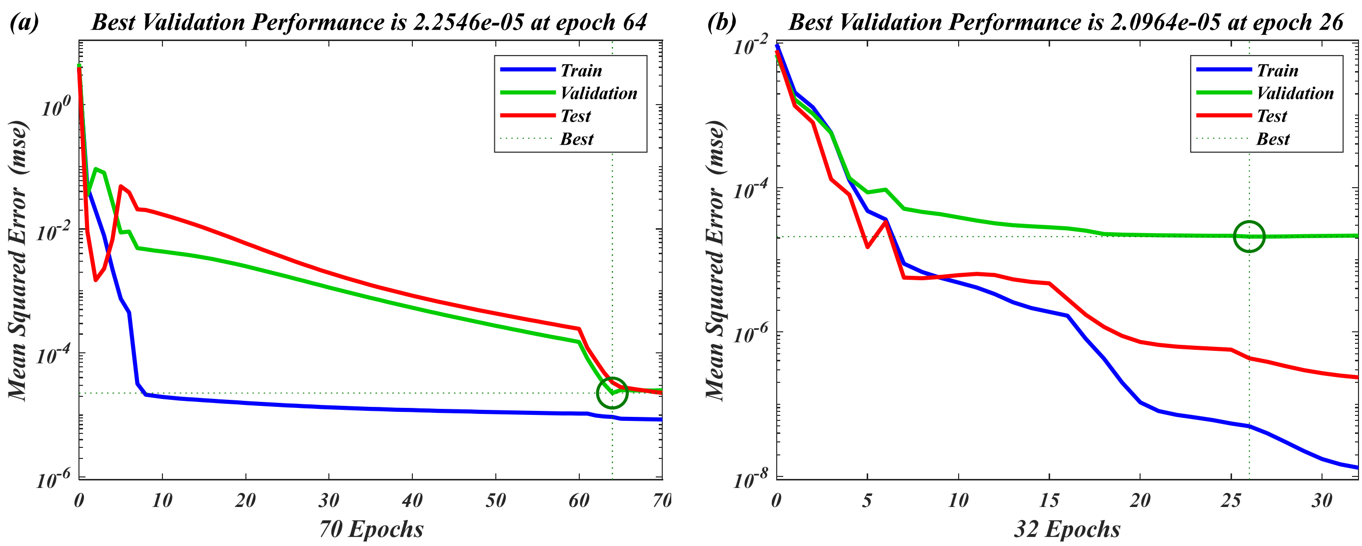

Figure 4. Training performance graph for (**a**) skin friction factor and (**b**) heat and mass transfer rate.

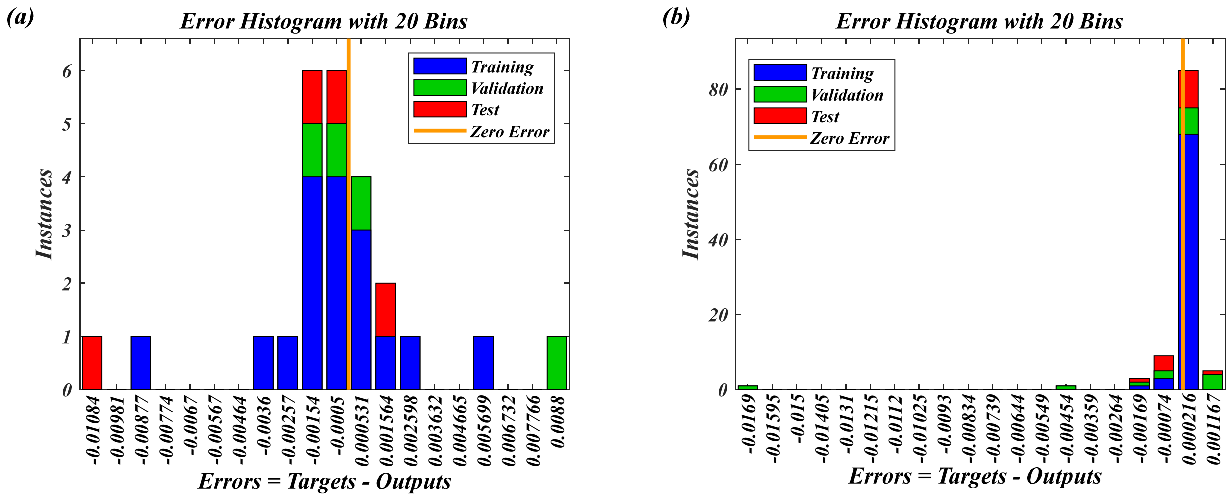

Figure 5. Error histogram graph for (**a**) skin friction factor and (**b**) heat and mass transfer rate.

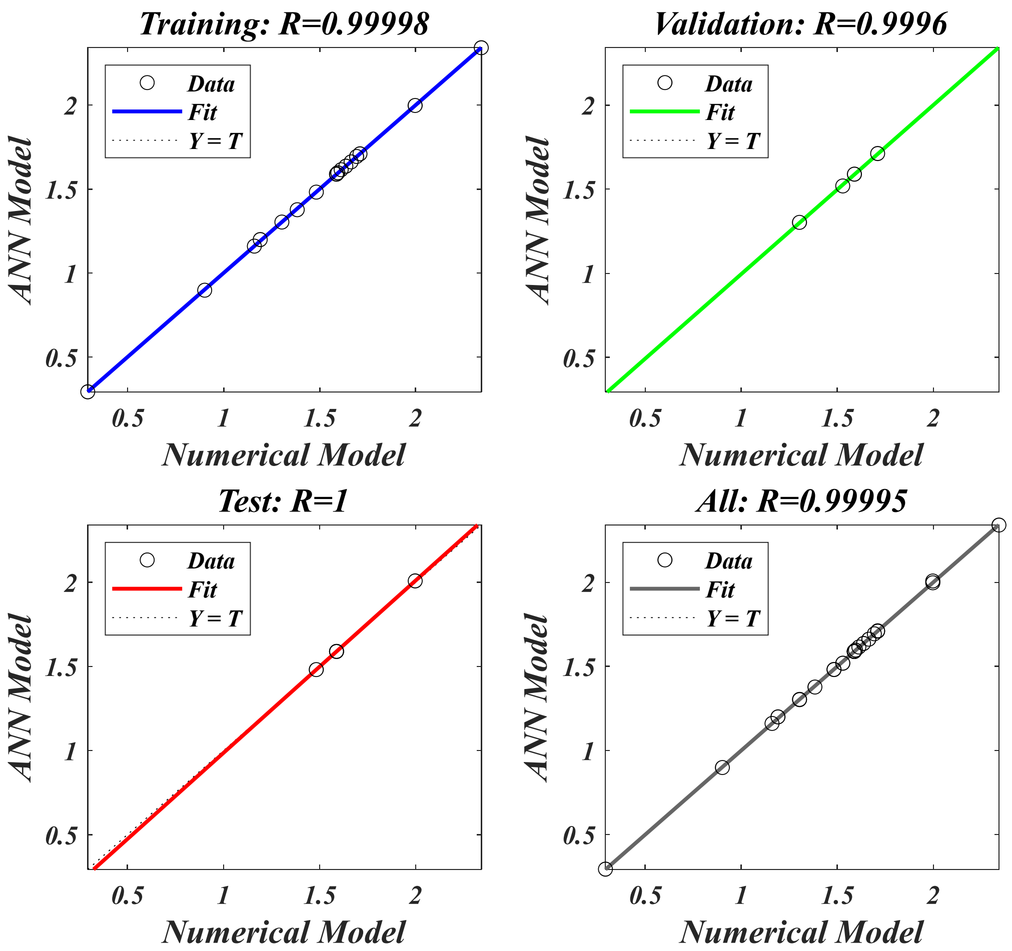

Figure 6. Numerical and ANN model for skin friction factor.

The outcomes of the artificial neural network (ANN) model exhibit a remarkable concurrence with the figures derived from computational analysis. Tables 2–5 present the skin friction factor, heat transfer rate, and mass transfer rate magnetic parameter $(\beta_{mp} = 0.1, 0.2, 0.3)$, Weissenberg number $(We = 0.5, 2.0, 3.5)$, velocity slip parameter $(\alpha_s = 0.1, 0.3, 0.5)$, magnetic Prandtl number $(M_{mp} = 0.1, 0.3, 0.5)$, thermal radiation parameter $(Rd = 1.0, 2.0, 3.0)$, Dufour number $(D_r = 0.001, 0.005, 0.010)$, Biot number $(Bi = 0.1, 0.3, 0.5)$, thermophoresis parameter $(N_T = 0.001, 0.005, 0.010)$, Brownian motion parameter ($N_B = 0.1, 0.2, 0.3$), Soret number ($S_r = 0.1, 0.5, 1.0$), chemical reaction parameter ($\gamma = 0.0, 1.0, 2.0$), and Schmidt number ($Sc = 0.5, 1.0, 1.5$) values for a range of parameters. In addition to the quantitative results, the findings of the artificial neural network model are demonstrated to be favorable. Thus far, the findings of this investigation have indicated that the artificial neural network (ANN) is capable of accurately forecasting both skin friction and heat transfer rate.

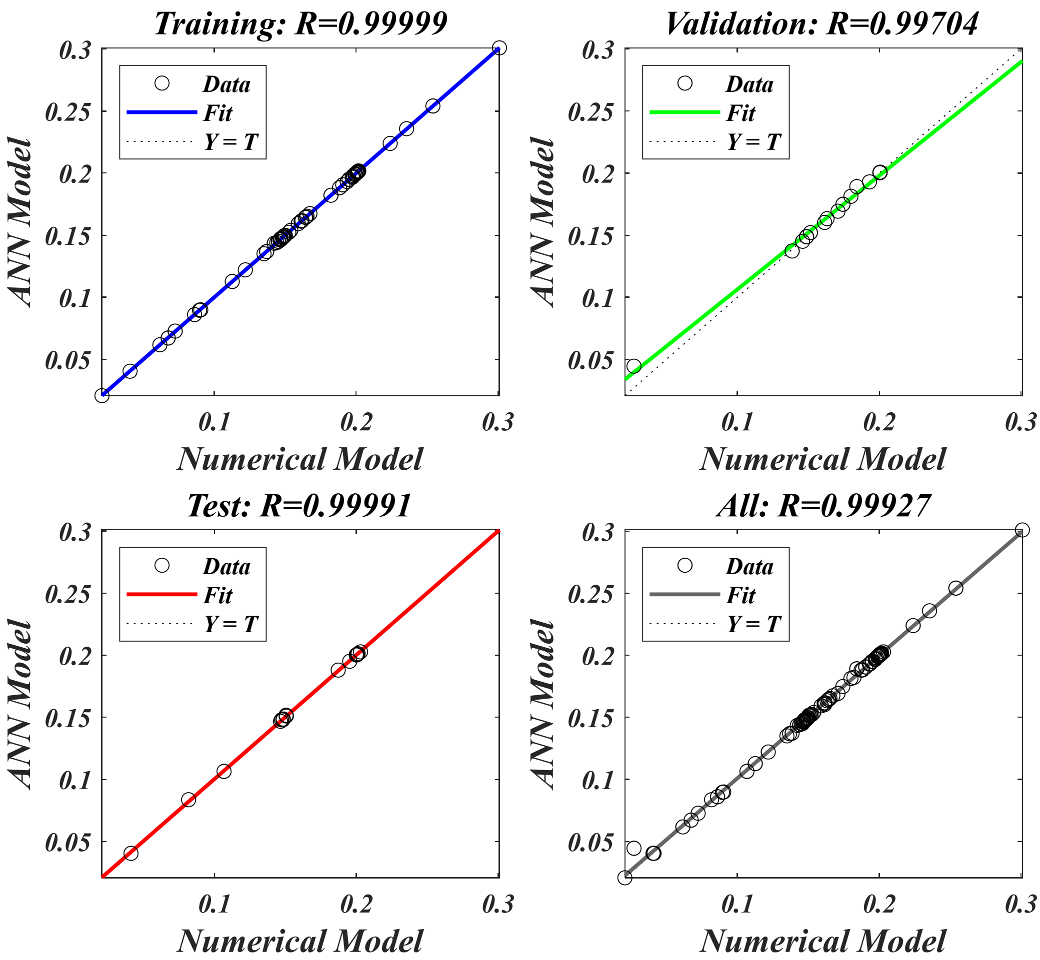

Figure 7. Numerical and ANN model for heat transfer rate and mass transfer rate.

Table 2. Effects of We, β_{mp}, and α_s on local skin friction coefficient C_f^*, dimensionless local rate of heat transfer Nu^*, and dimensionless local rate of mass transfer Sh^* over the wedge plate, wedge, and stagnation point.

	Parameter Values	Physical Quantities	Plate	Wedge	Stagnation Point
We	0.5	C_f^*	0.61098	1.15894	1.62372
		Nu^*	0.17579	0.19120	0.20069
		Sh^*	0.13759	0.13997	0.14865
	1.5	C_f^*	0.64079	1.24752	1.76215
		Nu^*	0.17602	0.19160	0.20115
		Sh^*	0.13738	0.13956	0.14819
	2.5	C_f^*	0.68280	1.34075	1.88226
		Nu^*	0.17648	0.19216	0.20162
		Sh^*	0.13712	0.13924	0.14797

Table 2. *Cont.*

	Parameter Values	Physical Quantities	Plate	Wedge	Stagnation Point
β_{mp}	0.1	C_f^*	0.60769	1.14176	1.58952
		Nu^*	0.17581	0.19116	0.20062
		Sh^*	0.13763	0.14006	0.14880
	0.3	C_f^*	0.53777	1.03182	1.46035
		Nu^*	0.17341	0.18966	0.19966
		Sh^*	0.13769	0.13949	0.14766
	0.5	C_f^*	0.46320	0.89631	1.29484
		Nu^*	0.17038	0.18750	0.19825
		Sh^*	0.13787	0.13882	0.14612
α_s	0.1	C_f^*	0.62774	1.37457	2.16400
		Nu^*	0.16060	0.17898	0.19102
		Sh^*	0.14033	0.14040	0.14600
	0.4	C_f^*	0.61465	1.19645	1.71000
		Nu^*	0.17304	0.18928	0.19932
		Sh^*	0.13803	0.13991	0.14809
	0.7	C_f^*	0.59115	1.04187	1.38777
		Nu^*	0.18010	0.19385	0.20237
		Sh^*	0.13714	0.14048	0.15002

Table 3. Effects of B_i, N_T, N_B, D_r, and S_r on dimensionless local rate of heat transfer Nu^* and dimensionless local rate of mass transfer Sh^* over the wedge plate, wedge, and stagnation point.

	Parameter Values	Physical Quantities	Plate	Wedge	Stagnation Point
B_i	0.1	Nu^*	0.04254	0.04352	0.04406
		Sh^*	0.15246	0.15893	0.17031
	0.4	Nu^*	0.14697	0.15769	0.16414
		Sh^*	0.14085	0.14435	0.15382
	0.7	Nu^*	0.22673	0.25245	0.26896
		Sh^*	0.13191	0.13219	0.13939
N_T	0.01	Nu^*	0.16741	0.18669	0.19806
		Sh^*	0.10187	0.08966	0.08950
	0.02	Nu^*	0.13749	0.17012	0.18823
		Sh^*	0.10891	0.06094	0.04049
	0.03	Nu^*	0.08634	0.14125	0.17092
		Sh^*	0.21073	0.08891	0.02709
N_B	0.1	Nu^*	0.11288	0.15630	0.18007
		Sh^*	0.15873	0.15577	0.16153
	0.2	Nu^*	0.03178	0.09207	0.13861
		Sh^*	0.17854	0.17381	0.17441
	0.3	Nu^*	0.00284	0.03414	0.08648
		Sh^*	0.18389	0.18913	0.18987

Table 3. *Cont.*

	Parameter Values	Physical Quantities	Plate	Wedge	Stagnation Point
D_r	0.01	Nu^*	0.16430	0.18535	0.19741
		Sh^*	0.14148	0.14208	0.14992
	0.02	Nu^*	0.14719	0.17720	0.19314
		Sh^*	0.14749	0.14504	0.15149
	0.03	Nu^*	0.11976	0.16514	0.18724
		Sh^*	0.15770	0.14970	0.15381
S_r	0.1	Nu^*	0.17528	0.19078	0.20035
		Sh^*	0.14923	0.15465	0.16529
	0.4	Nu^*	0.17567	0.19106	0.20055
		Sh^*	0.14055	0.14372	0.15294
	0.7	Nu^*	0.17607	0.19135	0.20075
		Sh^*	0.13174	0.13270	0.14051

Table 4. Skin friction factor values for different α_s, We, β_{mp} and M_{mp}.

α_s	We	β_{mp}	M_{mp}	C_f^*		
				NM	ANN	Error
0	0.1	0.1	0.1	2.341742	2.341054	6.87×10^{-4}
0.2	0.1	0.1	0.1	1.997203	1.997393	1.90×10^{-4}
0.4	0.1	0.1	0.1	1.710001	1.709799	2.02×10^{-4}
0.6	0.1	0.1	0.1	1.482665	1.482392	2.72×10^{-4}
0.8	0.1	0.1	0.1	1.303260	1.302654	6.06×10^{-4}
0.5	0.2	0.1	0.1	1.594459	1.597219	2.76×10^{-3}
0.5	0.4	0.1	0.1	1.612127	1.615347	3.22×10^{-3}
0.5	0.6	0.1	0.1	1.636474	1.636499	2.52×10^{-5}
0.5	0.8	0.1	0.1	1.663976	1.662062	1.91×10^{-3}
0.5	1	0.1	0.1	1.692508	1.694016	1.51×10^{-3}
0.5	0.1	0.2	0.1	1.528476	1.519159	9.32×10^{-3}
0.5	0.1	0.4	0.1	1.383355	1.377509	5.85×10^{-3}
0.5	0.1	0.6	0.1	1.190723	1.199874	9.15×10^{-3}
0.5	0.1	0.8	0.1	0.901431	0.898421	3.01×10^{-3}
0.5	0.1	1	0.1	0.292491	0.294073	1.58×10^{-3}
0.5	0.1	0.1	0.2	1.589078	1.589140	6.21×10^{-5}
0.5	0.1	0.1	0.4	1.588526	1.589259	7.32×10^{-4}
0.5	0.1	0.1	0.6	1.588166	1.589272	1.11×10^{-3}
0.5	0.1	0.1	0.8	1.587900	1.589409	1.51×10^{-3}
0.5	0.1	0.1	1	1.587689	1.588979	1.29×10^{-3}

Table 5. Heat transfer rate and mass transfer rate for different α_s, We, β_{mp}, M_{mp}, Rd, N_T, N_B, D_r, S_r, $\gamma$and B_i.

α_s	We	β_{mp}	M_{mp}	Rd	N_T	N_B	D_r	S_r	γ	B_i	Nu^*			Sh^*		
											NM	ANN	Error	NM	ANN	Error
0	0.1	0.1	0.1	1	0.001	0.01	0.001	0.5	1	0.5	0.1842	0.1891	4.90×10^{-3}	0.1460	0.1450	9.62×10^{-4}
0.2	0.1	0.1	0.1	1	0.001	0.01	0.001	0.5	1	0.5	0.1950	0.1950	6.98×10^{-6}	0.1466	0.1466	2.84×10^{-5}
0.4	0.1	0.1	0.1	1	0.001	0.01	0.001	0.5	1	0.5	0.1993	0.1992	8.00×10^{-5}	0.1481	0.1481	2.37×10^{-5}
0.6	0.1	0.1	0.1	1	0.001	0.01	0.001	0.5	1	0.5	0.2016	0.2015	6.08×10^{-5}	0.1494	0.1496	1.18×10^{-4}
0.5	0.2	0.1	0.1	1	0.001	0.01	0.001	0.5	1	0.5	0.2006	0.2007	6.93×10^{-5}	0.1488	0.1487	7.70×10^{-5}
0.5	0.4	0.1	0.1	1	0.001	0.01	0.001	0.5	1	0.5	0.2007	0.2006	5.71×10^{-5}	0.1487	0.1486	1.17×10^{-4}
0.5	0.6	0.1	0.1	1	0.001	0.01	0.001	0.5	1	0.5	0.2007	0.2006	1.54×10^{-4}	0.1486	0.1486	2.39×10^{-5}
0.5	0.8	0.1	0.1	1	0.001	0.01	0.001	0.5	1	0.5	0.2008	0.2008	4.59×10^{-5}	0.1485	0.1486	1.55×10^{-4}
0.5	0.1	0.2	0.1	1	0.001	0.01	0.001	0.5	1	0.5	0.2002	0.2002	5.13×10^{-5}	0.1483	0.1481	1.86×10^{-4}
0.5	0.1	0.4	0.1	1	0.001	0.01	0.001	0.5	1	0.5	0.1990	0.1989	1.37×10^{-4}	0.1470	0.1466	3.95×10^{-4}
0.5	0.1	0.6	0.1	1	0.001	0.01	0.001	0.5	1	0.5	0.1972	0.1967	5.75×10^{-4}	0.1451	0.1450	1.09×10^{-4}
0.5	0.1	0.8	0.1	1	0.001	0.01	0.001	0.5	1	0.5	0.1936	0.1932	4.11×10^{-4}	0.1422	0.1435	1.25×10^{-3}
0.5	0.1	0.1	0.2	1	0.001	0.01	0.001	0.5	1	0.5	0.2006	0.2006	3.22×10^{-6}	0.1488	0.1488	1.56×10^{-5}
0.5	0.1	0.1	0.4	1	0.001	0.01	0.001	0.5	1	0.5	0.2006	0.2005	1.23×10^{-4}	0.1488	0.1487	4.70×10^{-5}
0.5	0.1	0.1	0.6	1	0.001	0.01	0.001	0.5	1	0.5	0.2006	0.2004	1.93×10^{-4}	0.1488	0.1488	2.24×10^{-5}
0.5	0.1	0.1	0.8	1	0.001	0.01	0.001	0.5	1	0.5	0.2006	0.2005	5.83×10^{-5}	0.1488	0.1489	8.30×10^{-5}
0.5	0.1	0.1	0.1	0.1	0.001	0.01	0.001	0.5	1	0.5	0.0207	0.0207	2.97×10^{-5}	0.1463	0.1461	1.15×10^{-4}
0.5	0.1	0.1	0.1	0.2	0.001	0.01	0.001	0.5	1	0.5	0.0412	0.0404	7.99×10^{-4}	0.1466	0.1468	1.46×10^{-4}
0.5	0.1	0.1	0.1	0.3	0.001	0.01	0.001	0.5	1	0.5	0.0616	0.0617	1.40×10^{-4}	0.1469	0.1474	4.23×10^{-4}
0.5	0.1	0.1	0.1	0.4	0.001	0.01	0.001	0.5	1	0.5	0.0818	0.0836	1.86×10^{-3}	0.1473	0.1480	7.13×10^{-4}
0.5	0.1	0.1	0.1	1	0.01	0.01	0.001	0.5	1	0.5	0.1981	0.1980	2.63×10^{-5}	0.0895	0.0896	5.67×10^{-5}
0.5	0.1	0.1	0.1	1	0.02	0.01	0.001	0.5	1	0.5	0.1882	0.1882	5.24×10^{-6}	0.0405	0.0404	8.69×10^{-5}
0.5	0.1	0.1	0.1	1	0.03	0.01	0.001	0.5	1	0.5	0.1709	0.1693	1.64×10^{-3}	0.0271	0.0445	1.74×10^{-2}
0.5	0.1	0.1	0.1	1	0.04	0.01	0.001	0.5	1	0.5	0.1463	0.1463	3.01×10^{-5}	0.0674	0.0672	2.13×10^{-4}
0.5	0.1	0.1	0.1	1	0.001	0.10	0.001	0.5	1	0.5	0.1801	0.1813	1.25×10^{-3}	0.1615	0.1603	1.26×10^{-3}
0.5	0.1	0.1	0.1	1	0.001	0.15	0.001	0.5	1	0.5	0.1618	0.1617	5.48×10^{-5}	0.1673	0.1674	3.81×10^{-5}
0.5	0.1	0.1	0.1	1	0.001	0.20	0.001	0.5	1	0.5	0.1386	0.1372	1.41×10^{-3}	0.1744	0.1749	4.53×10^{-4}
0.5	0.1	0.1	0.1	1	0.001	0.25	0.001	0.5	1	0.5	0.1126	0.1127	8.95×10^{-5}	0.1822	0.1822	3.52×10^{-5}
0.5	0.1	0.1	0.1	1	0.001	0.01	0.01	0.5	1	0.5	0.1974	0.1972	1.59×10^{-4}	0.1499	0.1499	4.22×10^{-5}
0.5	0.1	0.1	0.1	1	0.001	0.01	0.015	0.5	1	0.5	0.1954	0.1952	2.36×10^{-4}	0.1507	0.1510	3.74×10^{-4}
0.5	0.1	0.1	0.1	1	0.001	0.01	0.02	0.5	1	0.5	0.1931	0.1929	2.09×10^{-4}	0.1515	0.1520	5.18×10^{-4}
0.5	0.1	0.1	0.1	1	0.001	0.01	0.025	0.5	1	0.5	0.1905	0.1906	5.21×10^{-5}	0.1525	0.1523	2.20×10^{-4}
0.5	0.1	0.1	0.1	1	0.001	0.01	0.001	0.1	1	0.5	0.2003	0.2002	1.18×10^{-4}	0.1653	0.1653	3.98×10^{-5}
0.5	0.1	0.1	0.1	1	0.001	0.01	0.001	0.15	1	0.5	0.2004	0.2003	5.56×10^{-5}	0.1632	0.1633	4.70×10^{-5}
0.5	0.1	0.1	0.1	1	0.001	0.01	0.001	0.2	1	0.5	0.2004	0.2004	2.99×10^{-6}	0.1612	0.1613	1.11×10^{-4}
0.5	0.1	0.1	0.1	1	0.001	0.01	0.001	0.25	1	0.5	0.2005	0.2005	5.38×10^{-5}	0.1591	0.1593	1.52×10^{-4}
0.5	0.1	0.1	0.1	1	0.001	0.01	0.001	0.5	0	0.5	0.2017	0.2017	1.01×10^{-5}	0.0723	0.0727	4.06×10^{-4}
0.5	0.1	0.1	0.1	1	0.001	0.01	0.001	0.5	0.2	0.5	0.2015	0.2014	4.18×10^{-5}	0.0904	0.0898	5.45×10^{-4}
0.5	0.1	0.1	0.1	1	0.001	0.01	0.001	0.5	0.4	0.5	0.2012	0.2013	2.11×10^{-5}	0.1067	0.1064	3.08×10^{-4}
0.5	0.1	0.1	0.1	1	0.001	0.01	0.001	0.5	0.6	0.5	0.2010	0.2011	9.63×10^{-5}	0.1218	0.1220	2.45×10^{-4}
0.5	0.1	0.1	0.1	1	0.001	0.01	0.001	0.5	1	0.2	0.0860	0.0860	1.65×10^{-5}	0.1646	0.1645	3.64×10^{-5}
0.5	0.1	0.1	0.1	1	0.001	0.01	0.001	0.5	1	0.4	0.1641	0.1643	1.30×10^{-4}	0.1538	0.1539	1.01×10^{-4}
0.5	0.1	0.1	0.1	1	0.001	0.01	0.001	0.5	1	0.6	0.2355	0.2358	2.56×10^{-4}	0.1440	0.1441	7.48×10^{-5}
0.5	0.1	0.1	0.1	1	0.001	0.01	0.001	0.5	1	0.8	0.3010	0.3010	6.59×10^{-5}	0.1350	0.1350	5.53×10^{-5}

4. Results and Discussion

This section is intended to demonstrate double-diffusive convection in radiative flow of Carreau nanofluid over three geometries (plate, wedge, and stagnation point) with induced magnetic field. In this section, the physical importance of velocities $(f'(\eta))$, induced magnetic field $(g'(\eta))$, temperature $(\theta(\eta))$, concentration $(\phi(\eta))$, skin friction $\left(C_f^*\right)$, Nusselt number (Nu^*), and mass transfer rate (Sh^*) are visualized and thoroughly discussed. Under specific boundary conditions, the dimensional version of the equations for flow, heat transport, and concentration is solved using the Runge–Kutta–Fehlberg for plate $(\beta = 0)$, wedge $(\beta = 0.5)$, and stagnation point $(\beta = 1.0)$ are shown as solid, dashed, and dotted lines in the comparison to the thermal radiative flow of ferromagnetic physical features over the three distinct geometries of the images, respectively. Comparing the results shows a significant degree of agreement, as shown in Table 6. This indicates that the accuracy of the numerical simulation's outcomes.

Table 6. Comparison of the present result (Nu^*) with the results of Lin and Lin [42] in the absences of We, β_{mp}, B_i, N_T, N_B, D_r, S_r, M_{mp}, n_k, We, Rd, S_r, and α_s.

Pr	Lin and Lin [42] Results			Present Results		
	$\beta_1 = 0$	$\beta_1 = 0.5$	$\beta_1 = 1.0$	$\beta_1 = 0$	$\beta_1 = 0.5$	$\beta_1 = 1.0$
1	0.372722	0.493968	0.640326	0.3727218	0.4939669	0.6403256
10	0.343388	0.477039	0.631365	0.3433875	0.4770383	0.6313644
100	0.339208	0.482208	0.644454	0.3392574	0.4822070	0.6444532
1000	0.338766	0.486599	0.653023	0.3387666	0.4865983	0.6530225

Figures 8 and 9 depict how the magnetic parameter $\left(\beta_{mp} = 0.1, 0.2, 0.3\right)$ affected the velocities $(f'(\eta))$ and induced magnetic field $(g'(\eta))$ profiles for β_1 = 0, 0.5, 1 s, respectively. It has been determined that the velocity profile $f'(\eta)$ decreases for higher values of β_{mp}. A similar nature is observed in the induced magnetic profile $(g'(\eta))$. The magnetic field deflects particles near the walls less than those in the center because the force acting on them is weaker. As a result, the magnetic field in the vicinity of the walls weakens while remaining strong at the wall's center. As a result, the magnetic field intensity in the velocity profile and induced magnetic field are decreased.

Figures 10 and 11 describe how the velocities $(f'(\eta))$ and induced magnetic field $(g'(\eta))$ profiles are influenced for the variations in Weissenberg number $(We = 0.5, 2.0, 3.5)$ blood nanofluid within the various geometries β_1 = 0, 0.5, 1. Note that the velocity profile diminishes for both $(f'(\eta))$ and $(g'(\eta))$ and rises for (We). The fluid's elasticity predominates as the Weissenberg number rises, and the blood-based fluid flow shows more prominent viscoelastic effects. For instance, the fluid may deform and stretch in reaction to the flow due to the elasticity, creating elastic stresses that hinder the flow. When compared to a fluid that is only viscous, this may result in the velocity profile being more wide and flat. The fluid's relaxation time, which is a component in the Weissenberg number definition, serves as a defining characteristic of this relaxation process. As a result, the Weissenberg number decreases and the fluid's elasticity becomes less prominent as the fluid moves downgradient, resulting in a narrower velocity profile that resembles the profile for a purely viscous fluid.

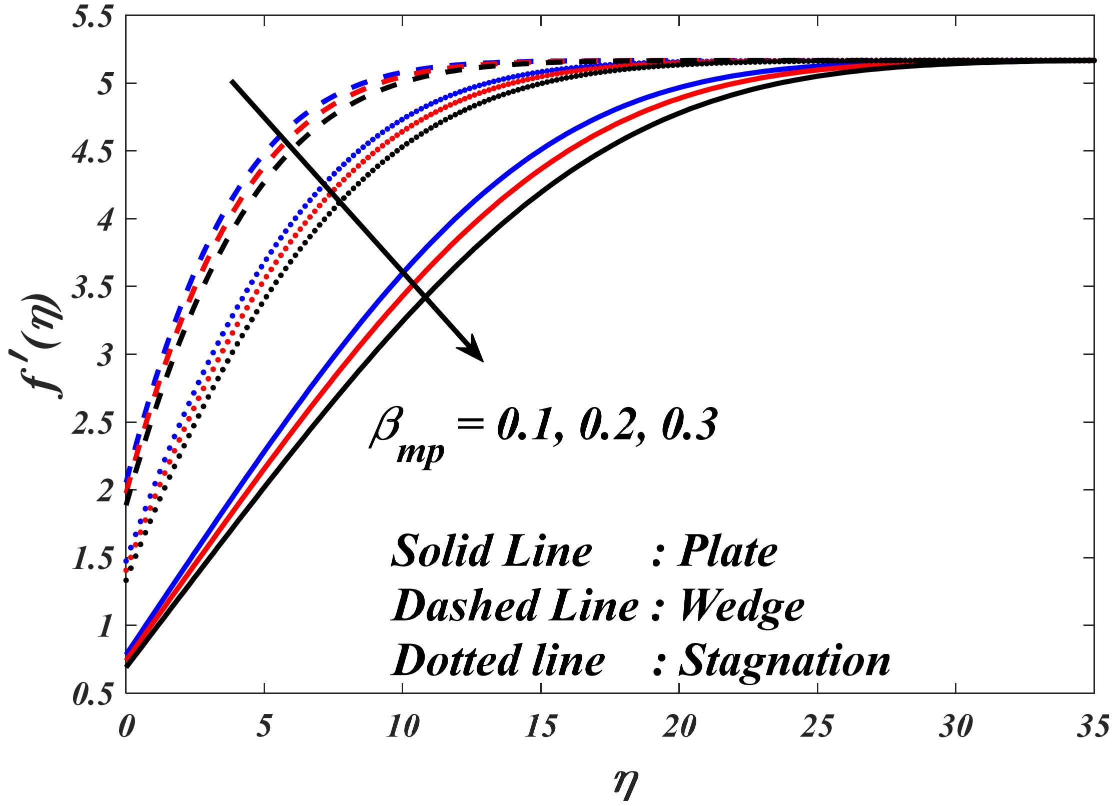

Figure 8. $f'(\eta)$ for increasing values of β_{mp}.

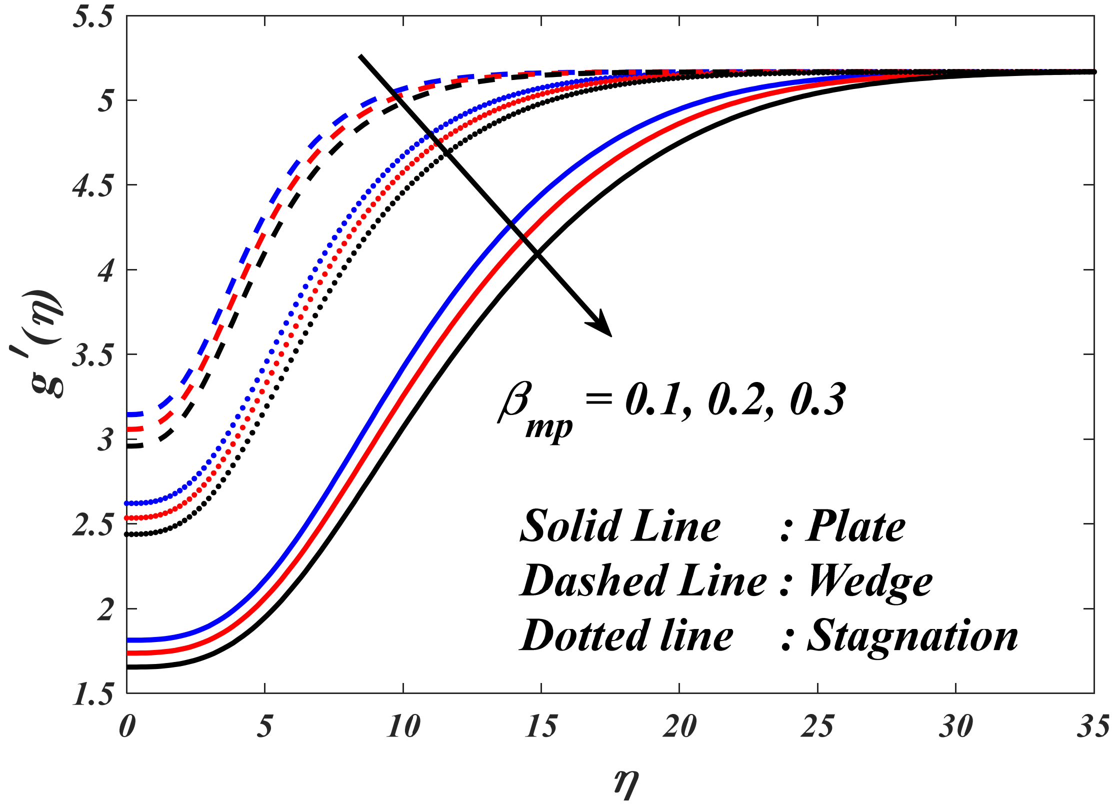

Figure 9. $g'(\eta)$ for increasing values of β_{mp}.

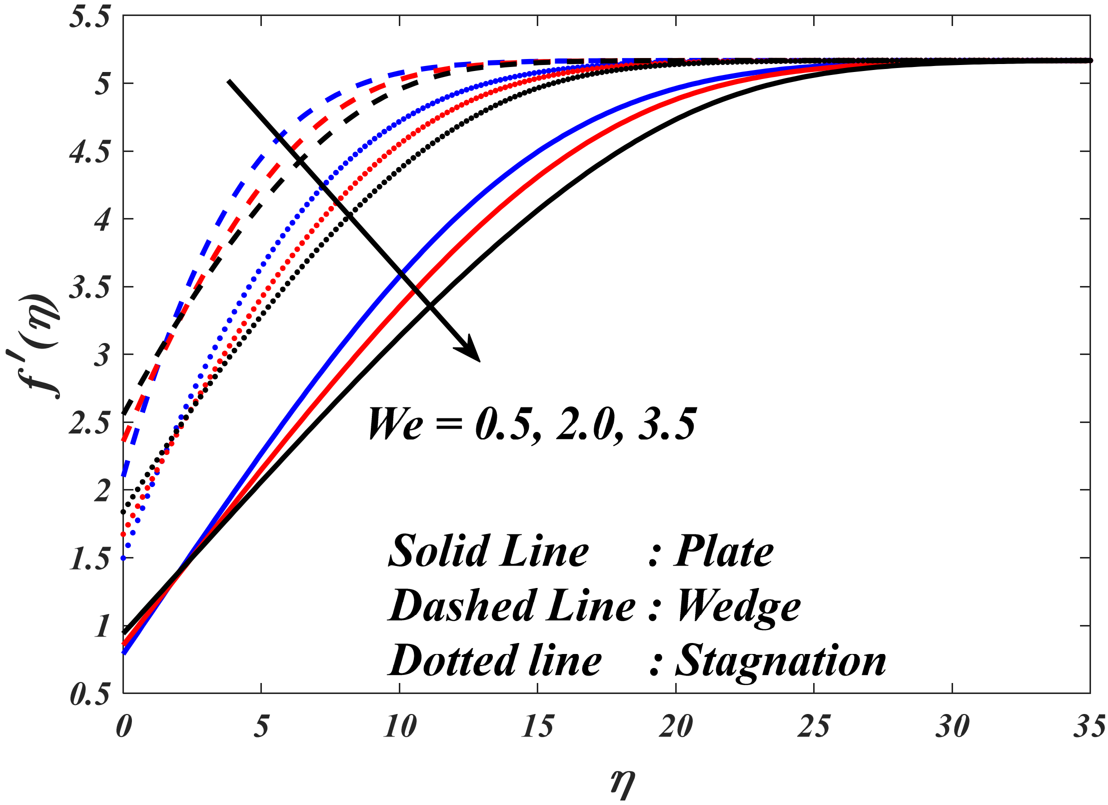

Figure 10. $f'(\eta)$ for increasing values of *We*.

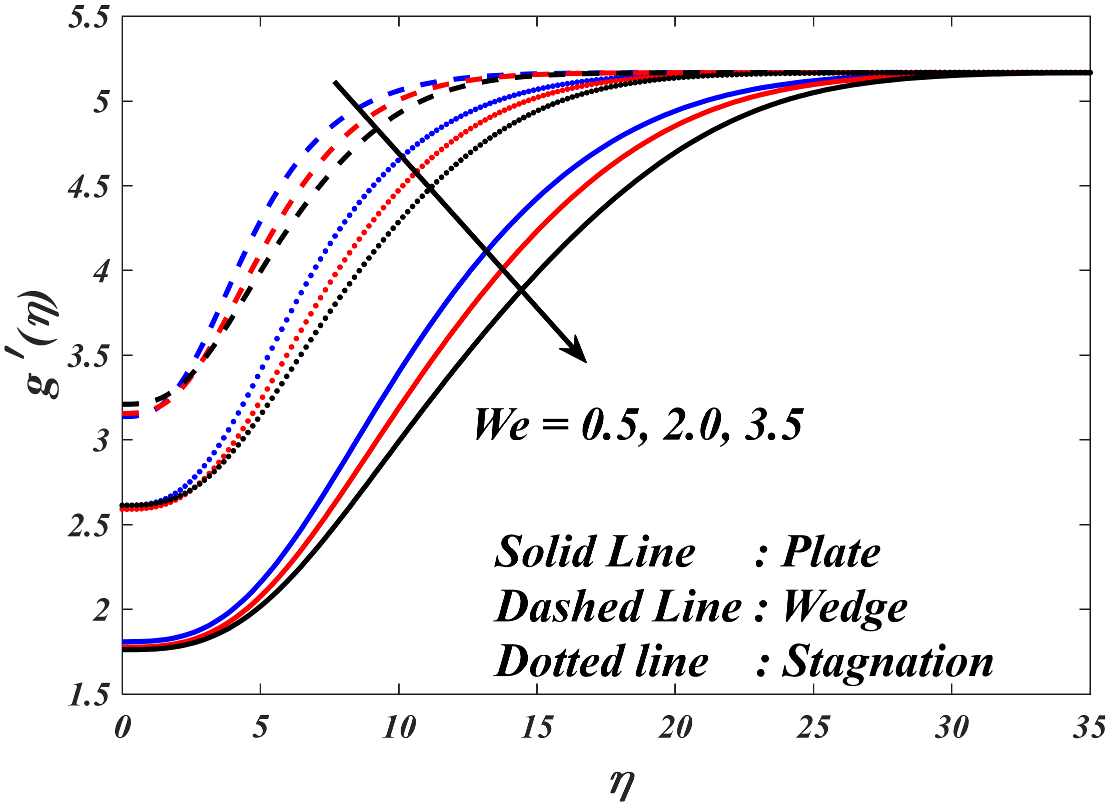

Figure 11. $g'(\eta)$ for increasing values of *We*.

The effect of the velocity slip parameter ($\alpha_s = 0.1, 0.3, 0.5$) on velocities $(f'(\eta))$, induced magnetic field $(g'(\eta))$ and temperature $(\theta(\eta))$ profiles changes are shown in Figures 12–14. These graphs indicate that increasing α_s values lead to an increase in $f'(\eta)$ and $g'(\eta)$ for the various geometries β_1 = 0, 0.5, and 1, but it is reduced for the temperature profile $(\theta(\eta))$. The blood fluid nanoparticles can interact with the solid surface to form a thin layer of adsorbed particles, which can change the surface's boundary conditions. The velocity slip parameter's value reflects the possibility of a slip velocity between the fluid and the surface. Due to the enhanced contacts between the nanoparticles and the surface, the slip velocity may rise as the fluid's nanoparticle concentration rises. The velocity slip parameter's value may rise as a result of this. In general, when the blood nanofluid temperature rises, the fluid's viscosity decreases and the blood cells and nanoparticles move through the fluid at a faster rate. The velocity slip parameter might rise as a result of the larger velocity differential between the fluid and the solid surface caused by the increasing velocity.

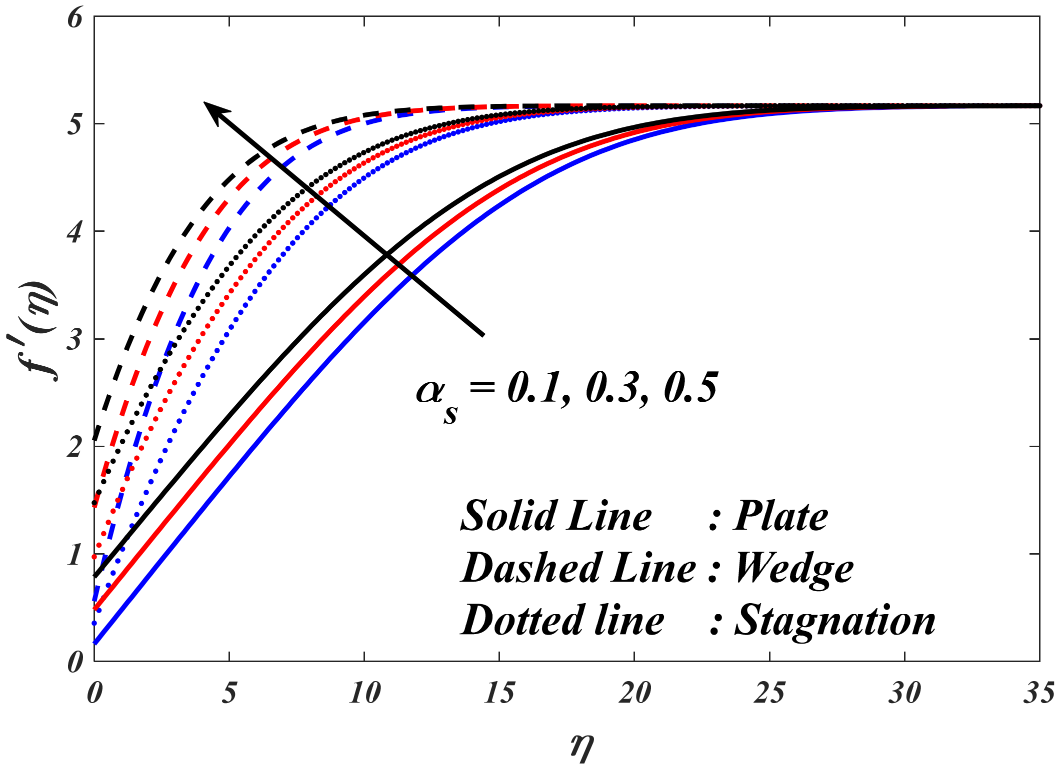

Figure 12. $f'(\eta)$ for increasing values of α_s.

Figure 15 shows the effect of different magnetic Prandtl numbers $(M_{mp} = 0.1, 0.3, 0.5)$ on the induced magnetic field $(g'(\eta))$ profile. It is acknowledged that the $g'(\eta)$ decreases when the magnetic Prandtl number M_{mp} increases. A blood-based nanofluid encounters the Lorentz force when an external magnetic field is introduced, which can cause the fluid to flow and produce heat transfer. The magnetic Prandtl number illustrates how important magnetic diffusion is in this process in relation to fluid viscosity. Additionally, the viscosity and thermal conductivity of the nanofluid may alter due to the nanoparticles, which may have an effect on the magnetic Prandtl number as a whole. Overall, the interaction between the magnetic nanoparticles, magnetic field, and fluid characteristics is the physical cause of the drop in magnetic Prandtl number in blood-based nanofluids under generated magnetic field profiles.

Figure 16 illustrates how the thermal radiation parameter $(Rd = 1.0, 2.0, 3.0)$ influence of temperature $(\theta(\eta))$ changes. According to this graph, the temperature $(\theta(\eta))$ rises with increasing Rd values. The interaction of the nanoparticles with thermal radiation, which can improve heat transfer and change the optical characteristics of the nanofluid, is the physical cause for the rise in radiation parameter in the blood-based nanofluid temperature profile.

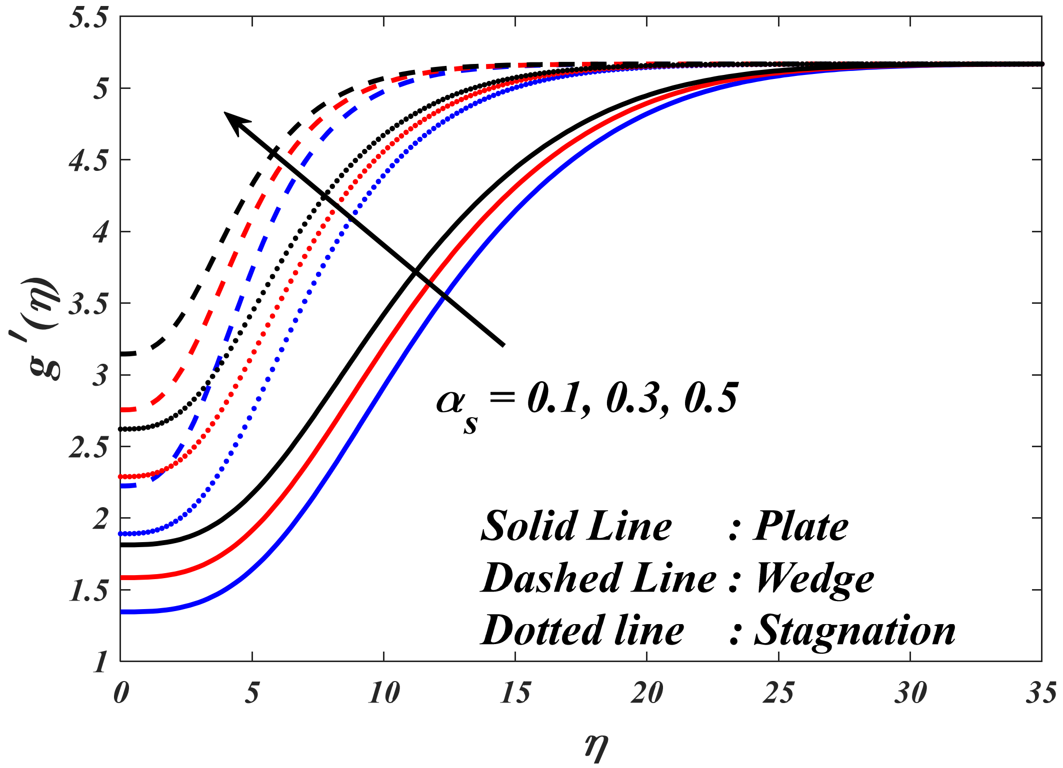

Figure 13. $g'(\eta)$ for increasing values of α_s.

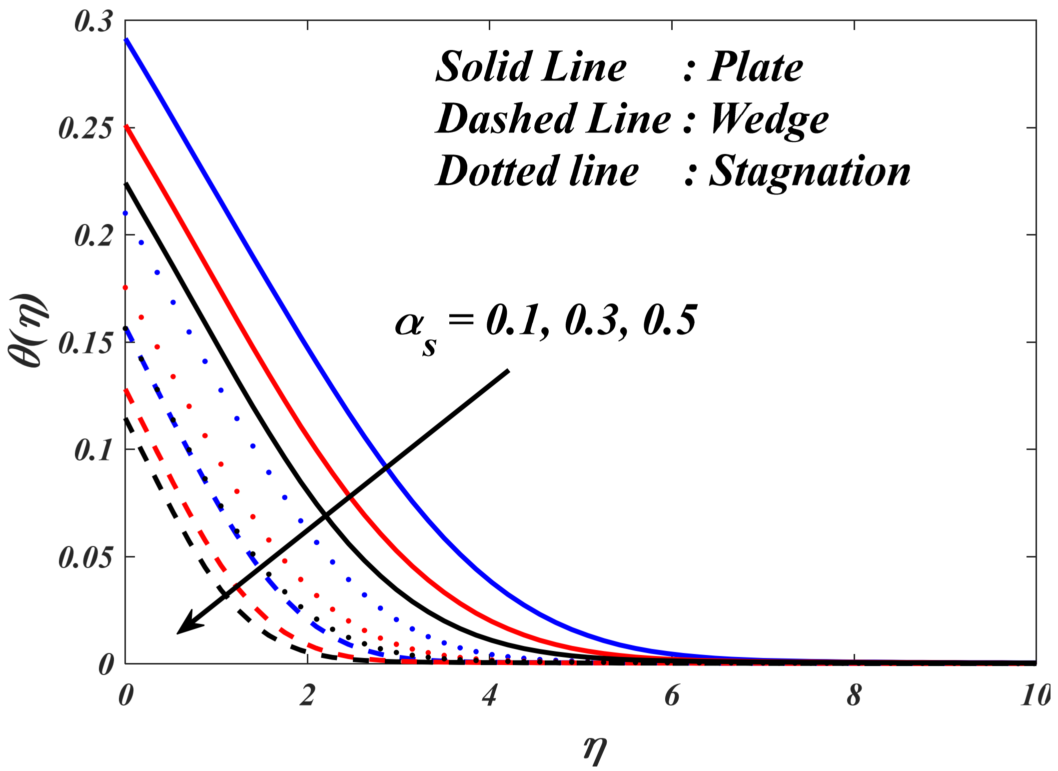

Figure 14. $\theta(\eta)$ for increasing values of α_s.

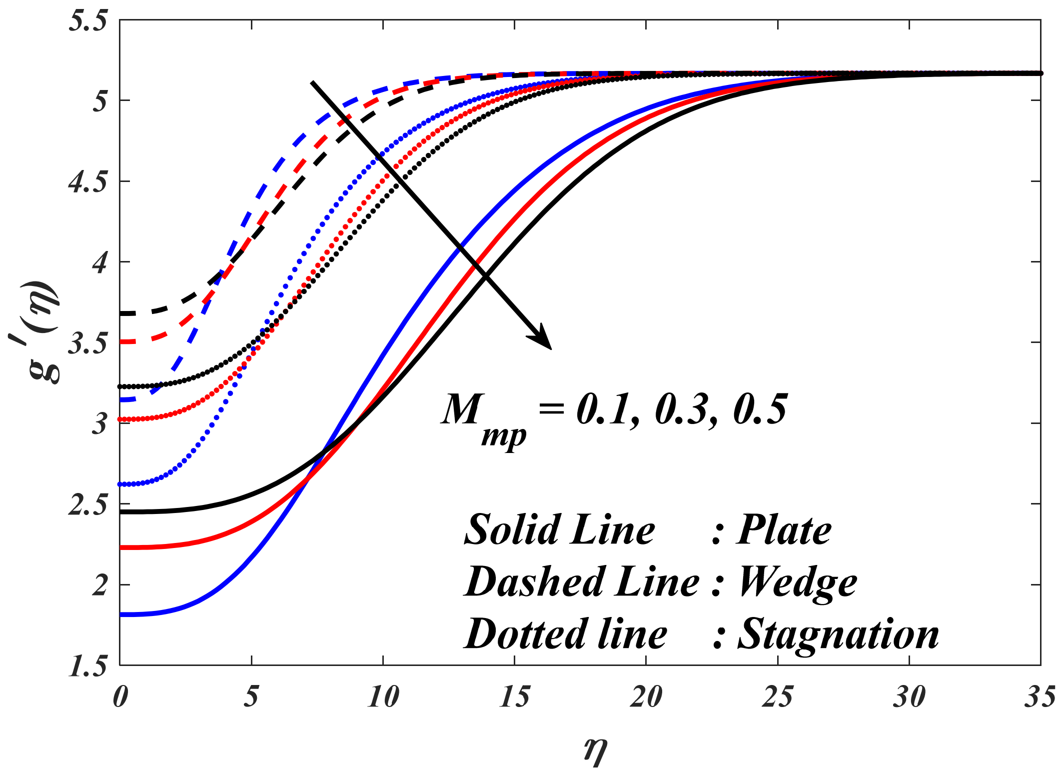

Figure 15. $g'(\eta)$ for increasing values of M_{mp}.

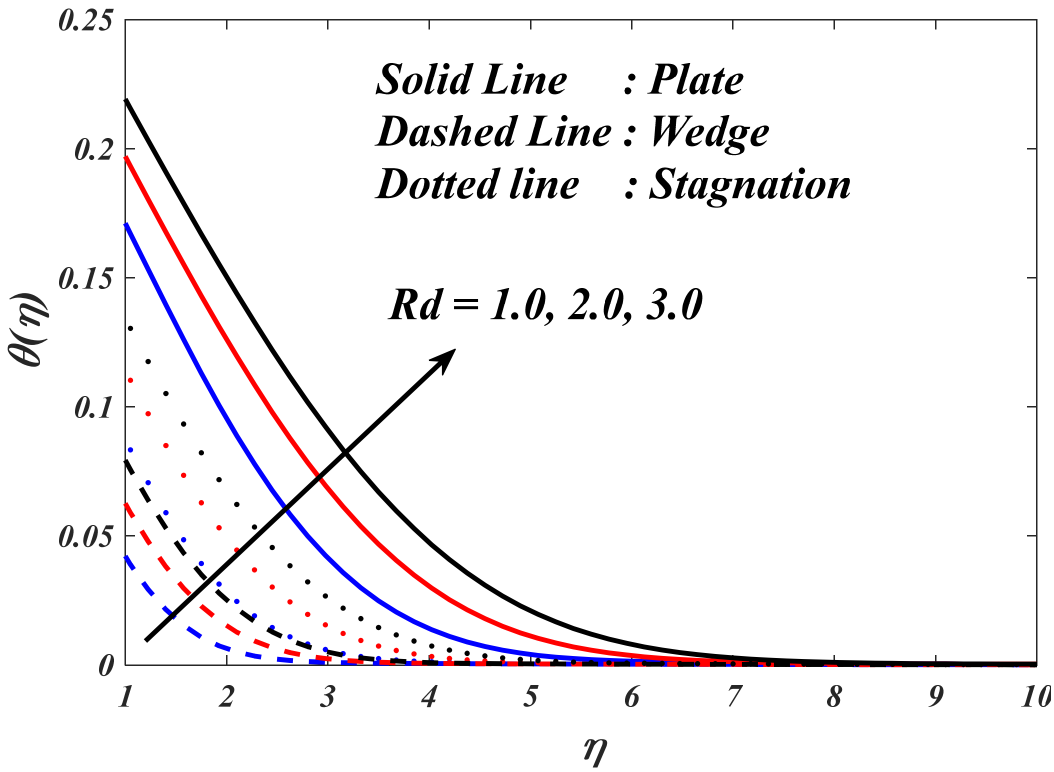

Figure 16. $\theta(\eta)$ for increasing values of Rd.

The fluctuations in $\theta(\eta)$ are shown in Figure 17 for different values of the Dufour number $(D_r = 0.001, 0.005, 0.010)$. It is detected that the $\theta(\eta)$ profiles increase by enhancing the Dufour number (D_r) values. When the temperature of the Dufour number rises, it indicates that thermal diffusion is occurring at a slower rate than the rate at which mass is transported through diffusion. This may occur because when the mixture's chemical composition varies with temperature, so do the components' diffusivities. This may lead to a rise in the Dufour number.

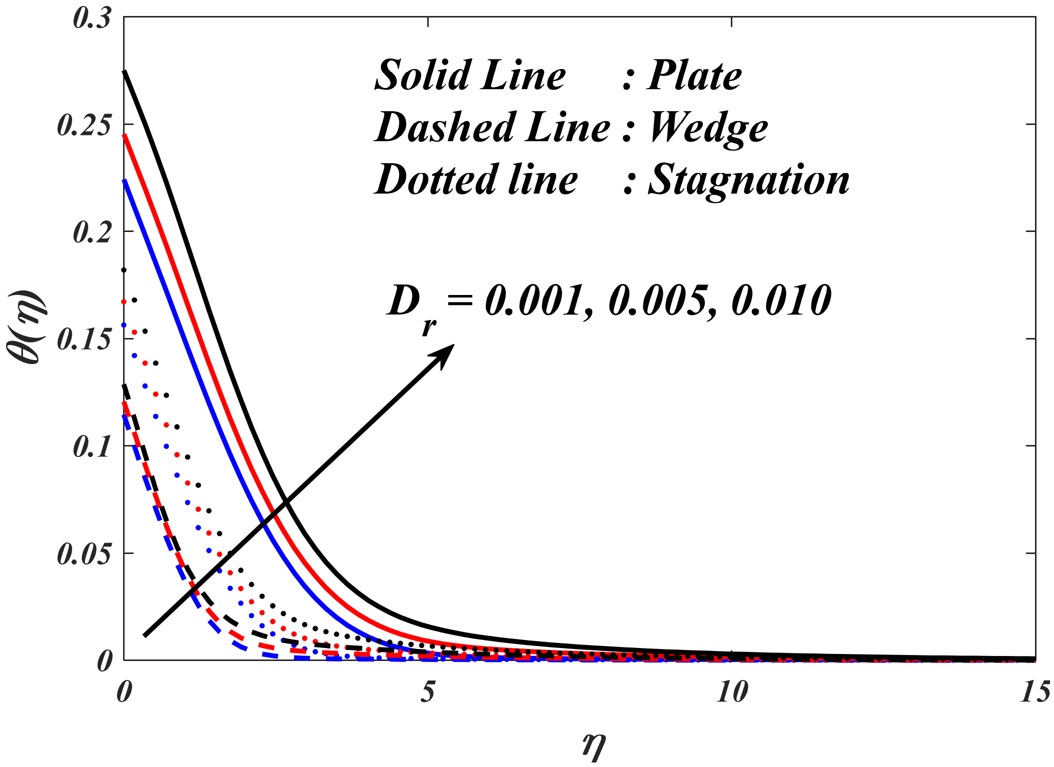

Figure 17. $\theta(\eta)$ for increasing values of D_r.

Figure 18 shows the temperature $(\theta(\eta))$ profile with different Biot number $(Bi = 0.1, 0.3, 0.5)$ values applied to the various geometries β_1 = 0, 0.5, 1. The temperature $(\theta(\eta))$ profile is increased when the Biot number (Bi) is increased. The Biot number is described as the relationship between a body's internal and exterior thermal resistances. In a temperature profile, an increasing Biot number indicates that the body's internal thermal resistance is rising compared to its exterior thermal resistance.

Figures 19 and 20 depict how the thermophoresis parameter $(N_T = 0.001, 0.005, 0.010)$ affected the temperature $(\theta(\eta))$ and concentration $(\phi(\eta))$ profiles for β_1 = 0, 0.5, 1 s, respectively. Figure 19 describes how the $\theta(\eta)$ influenced the three geometries to the variations in (Nt). It is observed that $\theta(\eta)$ intensification boosts (Nt). This is due to the action of thermophoresis, which draws large thermally conducting nanoparticles deeper into the fluid and exposes a stronger thermal boundary layer. The differences in a concentration profile $(\phi(\eta))$ for several thermophoresis values (Nt) are shown schematically in Figure 20. The $\theta(\eta)$ increases for superior values of (Nt). The wall slope of concentration profiles increases as the fluid concentration rises, nonetheless only partly.

The Brownian motion parameter $(N_B = 0.1, 0.2, 0.3)$ effect on the temperature profile $(\phi(\eta))$ and concentration profile $(\phi(\eta))$ in the case of β_1 = 0, 0.5, 1 was investigated with results shown in Figures 21 and 22. The effect of $\theta(\eta)$ on the changes in the Brownian motion parameter (N_B) is shown in Figure 21. It can be seen that $\theta(\eta)$ intensifications increase (N_B). Blood nanofluid flow collides with the basic liquid particles when there is an increase in the Brownian motion parameter. This results in an increase in temperature as well as an increase in the kinetic energy. The differences of a concentration profile $(\phi(\eta))$ for several values of Brownian motion (N_B) are shown schematically in Figure 22. The blood nanofluid of the concentration profile $(\phi(\eta))$ rises for superior values of (N_B). Physically, the random movement of the fluid particles improves with increasing Brownian motion, which increases heat generation and raises the fluid's temperature.

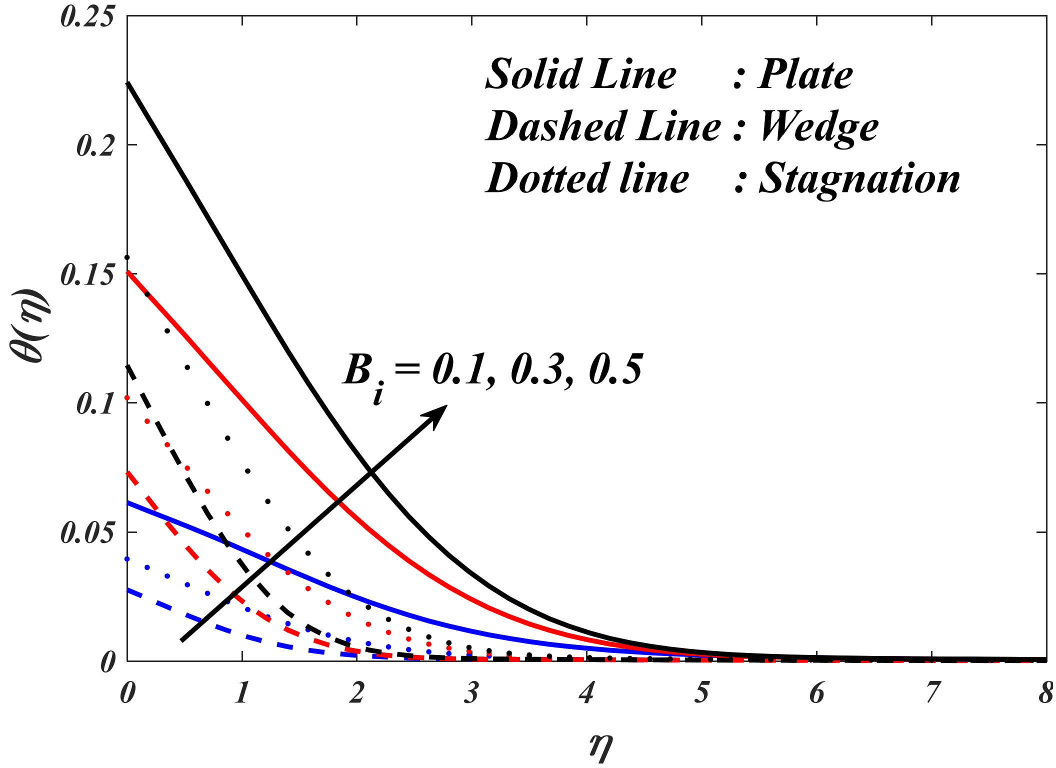

Figure 18. $\theta(\eta)$ for increasing values of B_i.

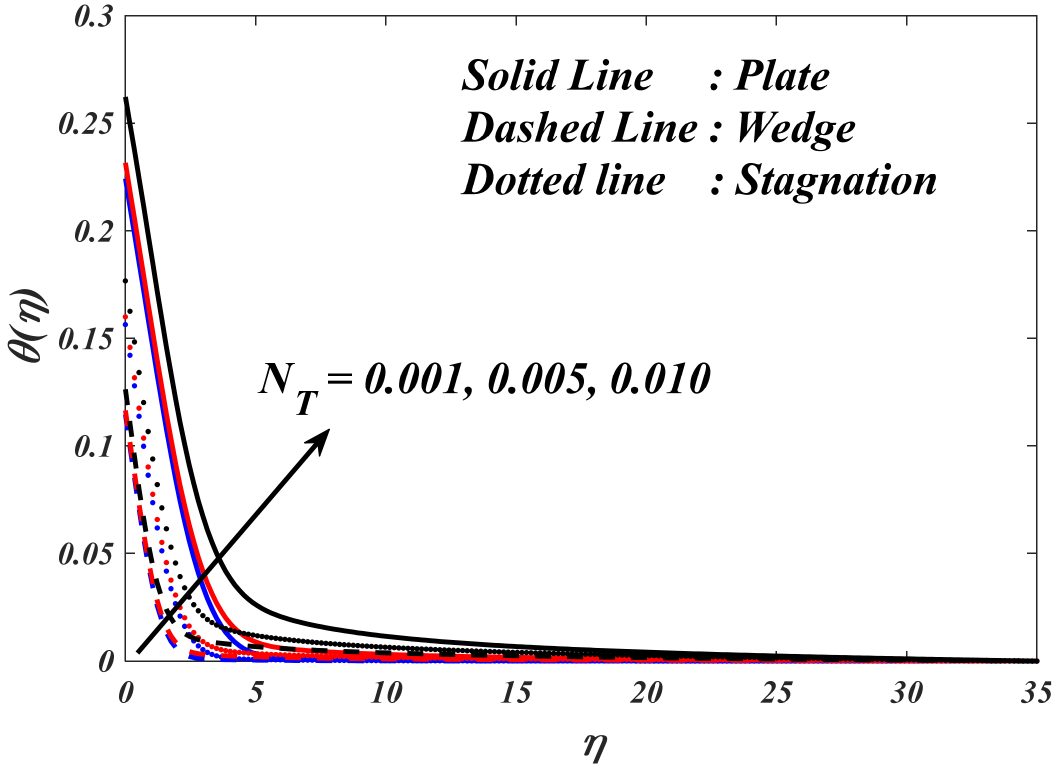

Figure 19. $\theta(\eta)$ for increasing values of N_T.

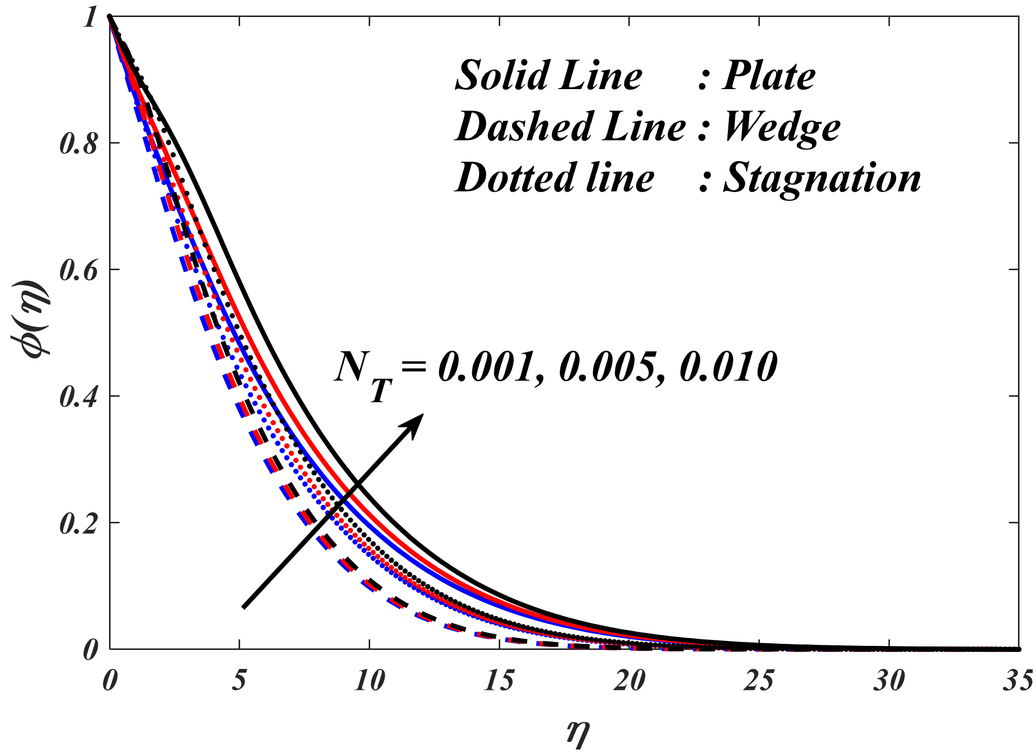

Figure 20. $\phi(\eta)$ for increasing values of N_T.

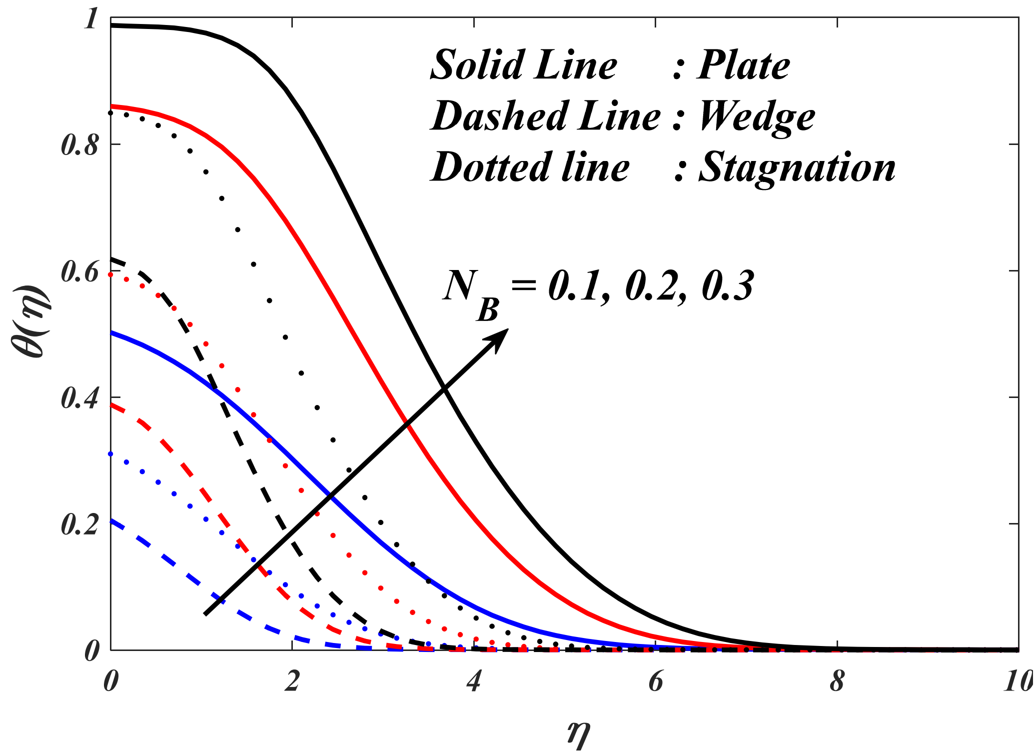

Figure 21. $\theta(\eta)$ for increasing values of N_B.

Figure 23 shows the concentration profile $(\phi(\eta))$ with various Soret number $(S_r = 0.1, 0.5, 1.0)$ values applied to the various geometries β_1 = 0, 0.5, 1. The concentration profile $(\phi(\eta))$ is increased when the Soret number (S_r) is increased. The relative rates of mass transport caused by temperature and concentration gradients in a fluid mixture are described by the dimensionless Soret number. The rate of mass transfer due to heat gradients increases relative to the rate of mass transport due to concentration gradients as the Soret number for a concentration profile in blood nanofluid flow increases.

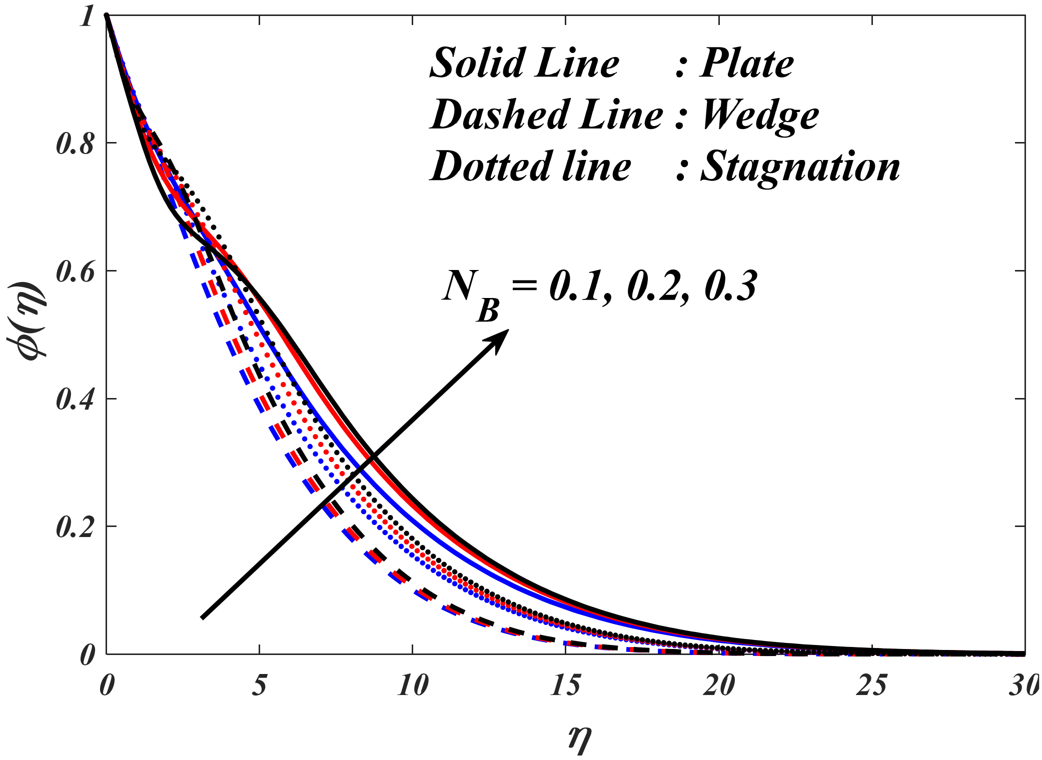

Figure 22. $\phi(\eta)$ for increasing values of N_B.

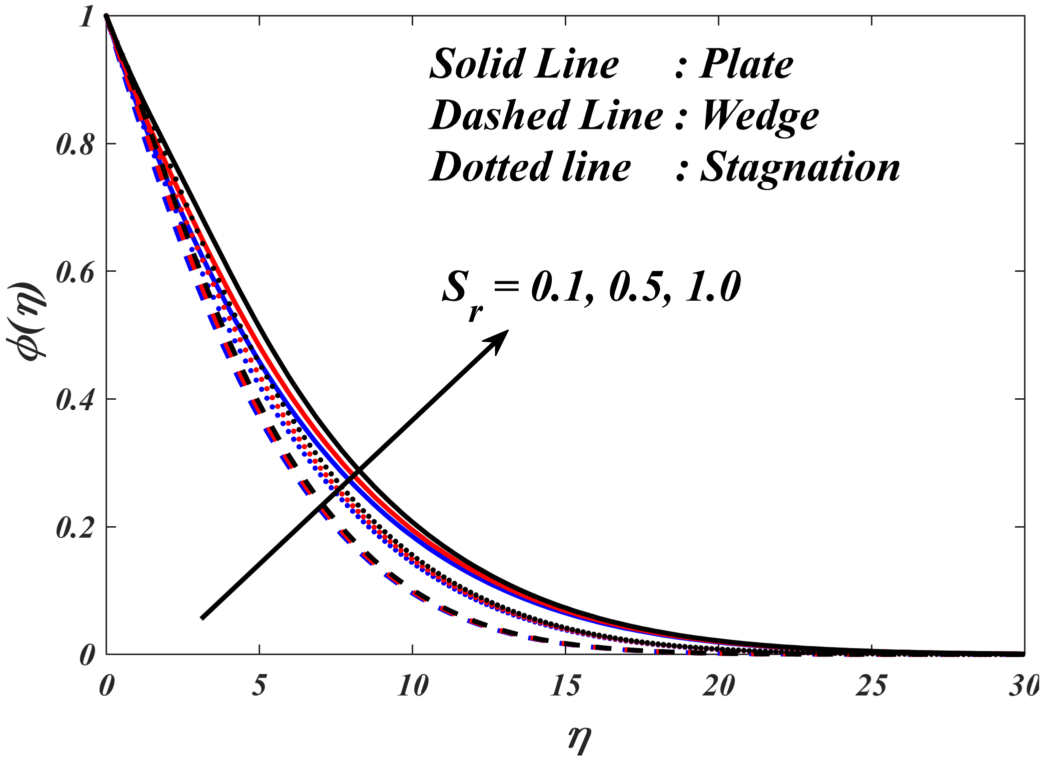

Figure 23. $\phi(\eta)$ for increasing values of S_r.

Figure 24 illustrates how the chemical reaction parameter ($\gamma = 0.0, 1.0, 2.0$) influences in thblood nanofluid flow with response to changes in the concentration profile ($\phi(\eta)$).

According to this graph, the concentration profile $(\phi(\eta))$ decays with increasing values of γ. The blood nanofluid flow concentration profiles show a drop in the chemical reaction parameter when compared to diffusion or convection, which indicates that the pace of chemical reactions is slowing.

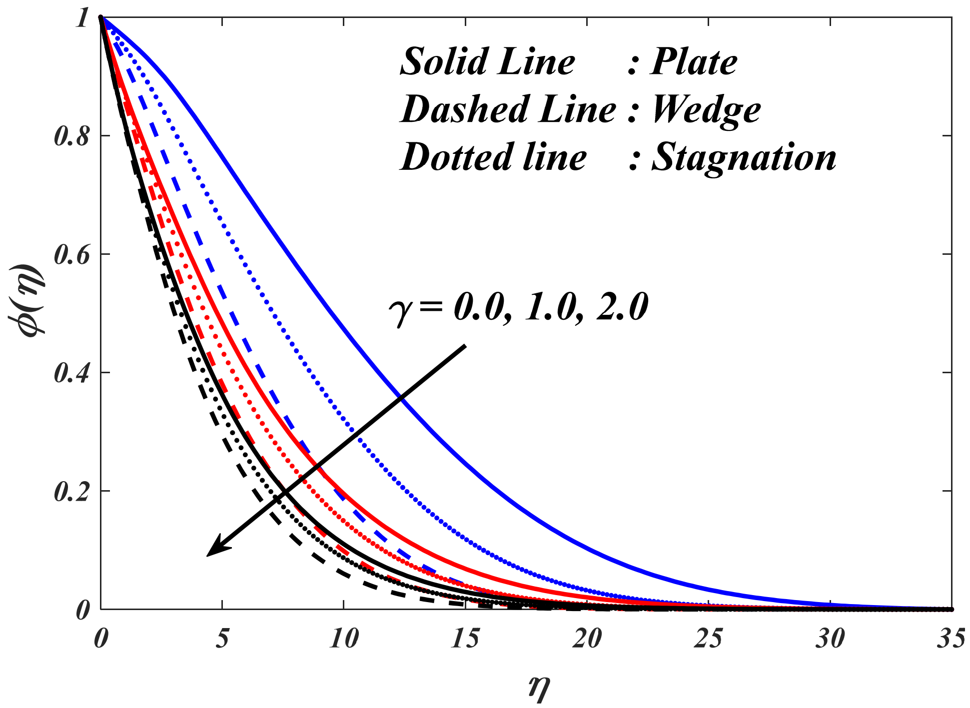

Figure 24. $\phi(\eta)$ for increasing values of γ.

Figure 25 illustrates how the Schmidt number $(Sc = 0.5, 1.0, 1.5)$ influences blood nanofluid flow with response to concentration profile $(\phi(\eta))$ changes. According to this graph, the concentration profile $(\phi(\eta))$ decays with increasing values of Sc.

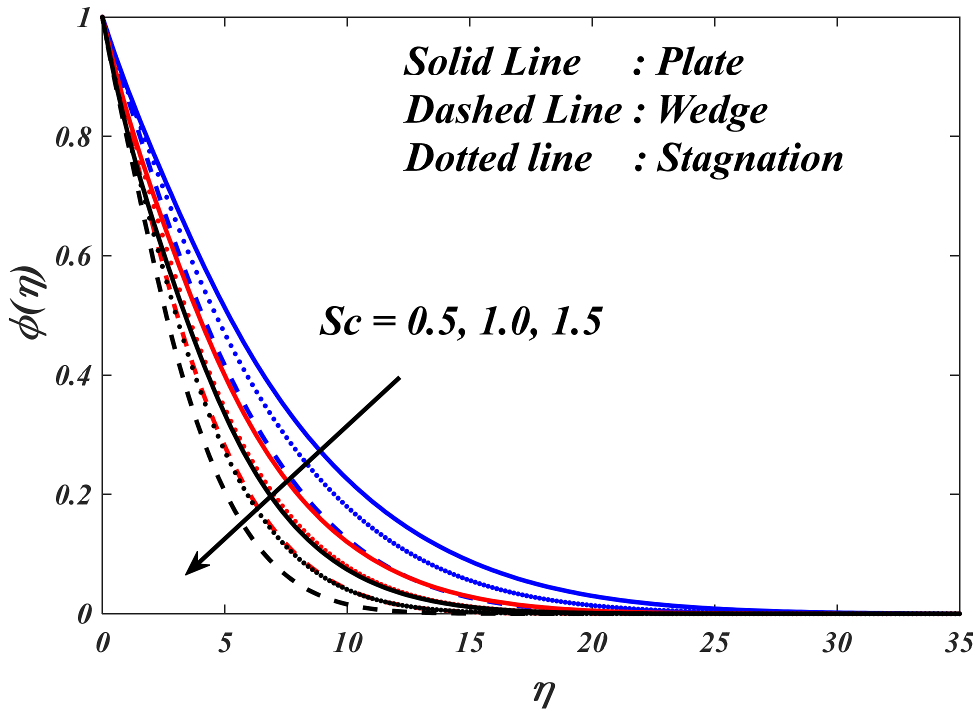

Figure 25. $\phi(\eta)$ for increasing values of Sc.

5. Conclusions

The purpose of this study is to illustrate double-diffusive convection for the fluid transport properties of blood-based Carreau nanofluid flow over three distinct geometries with an induced magnetic field. This type of theoretical investigation is extensively used in modern aspects of biological and chemical engineering, such as designing pumping devices for medical diagnostics, mixing samples at certain temperatures, and generating microscale flows using stimulus-responsive working fluids. The effect of important parameters like Weissenberg number, magnetic parameter, thermophoresis, Brownian motion, thermal radiation, Biot number, Soret number, and Dufour number are analyzed. The results are shown through two-dimensional graphs and tables. The following significant findings emerged from this investigation:

- The artificial neural network model does not require linearization, is fast convergent, and has a reduced processing cost.
- The velocity $f'(\eta)$ and induced magnetic profiles decrease for higher values of β_{mp} magnetic parameter in all the geometries.
- Velocity profile diminishes for both $(f'(\eta))$ and $(g'(\eta))$ given higher values of the Weissenberg number (We).
- Radiation, thermophoresis, and temperature ratio parameter increase corresponding to a rise in blood nanofluid temperature.
- The concentration profile $(\phi(\eta))$ decays with increasing values in the chemical reaction parameter (γ). The temperature $(\theta(\eta))$ profile is increased when the Biot number (Bi) is increased.
- Among the three geometries, the fluid flow over the plate has the largest heat transfer rate.

Author Contributions: Conceptualization, S.J. and S.R.R.R.; methodology, S.V.E.; software, H.T.B.; validation and writing—review and editing, J.C.; formal analysis and investigation, H.T.B. and S.V.E.; writing—original draft preparation, S.J. and S.R.R.R. All authors have read and agreed to the published version of the manuscript.

Funding: This work was supported by the Korea Environmental Industry and Technology Institute (KEITI), with a grant funded by the Korean Government, Ministry of Environment (The development of IoT-based technology for collecting and managing big data on environmental hazards and health effects), under grant RE202101551, and partially supported by the Institute of Information and Communications Technology Planning and Evaluation (IITP), funded by the Korean Government, Ministry of Science and ICT (MSIT) (Implementation of verification platform for ICT based environmental monitoring sensor), under grant 2019-0-00135.

Data Availability Statement: Not applicable.

Conflicts of Interest: On behalf of all authors, the corresponding author states that there are no conflict of interest.

Nomenclature

B_i	Biot number
c_{p_f}	specific heat of fluid
c_{p_p}	specific heat of particle
c_s	concentration susceptibility
C_w	nanoparticles concentration at the wall
C_∞	ambient nanoparticles concentration
D_B	Brownian diffusion coefficient
D_m	coefficient of mean diffusivity
D_r	Dufour number
D_T	thermophoresis diffusion coefficient
h_f	convective heat transfer coefficient
H_0	uniform upstream magnetic field

$H_1 \& H_2$	parallel and the normal direction of the applied magnetic field
k_T	thermal-diffusion ratio
k_f	thermal conductivity of fluid
k_1^*	mean absorption coefficient
K_r	dimensional chemical reaction parameter
L_1	velocity slip factor
m	Hartree pressure gradient parameter
M_{mp}	magnetic Prandtl number
N_T	thermophoresis parameter
N_B	Brownian motion parameter
n_k	power law index
Pr	Prandtl number
Rd	radiation parameter
S_r	Soret number
Sc	Schmidt number
T_∞	ambient nanoparticles temperature
T_w	nanoparticles temperature at the wall
T_m	fluid mean temperature
We	Weissenberg number
σ^*	Stefan–Boltzman constant
Γ	material parameter
μ_{mp}	magnetic permeability
ρ_f	density of the fluid
α_s	velocity slip parameter
β_{mp}	magnetic parameter
γ	chemical reaction parameter
μ_e	magnetic diffusivity
τ	ratio between particle and base fluid
ρ_p	density of the particle
α_f	thermal diffusivity of fluid

References

1. Sitamahalakshmi, V.; Reddy, G.V.R.; Falodun, B.O. Heat and Mass Transfer Effects on MHD Casson Fluid Flow of Blood in Stretching Permeable Vessel. *J. Appl. Nonlinear Dyn.* **2023**, *12*, 87–97. [CrossRef]
2. Ketchate, C.G.N.; Kapen, P.T.; Madiebie-Lambou, I.; Fokwa, D.; Chegnimonhan, V.; Tchinda, R.; Tchuen, G. Chemical reaction, Dufour and Soret effects on the stability of magnetohydrodynamic blood flow conveying magnetic nanoparticle in presence of thermal radiation: A biomedical application. *Heliyon* **2023**, *9*, e12962. [CrossRef] [PubMed]
3. Murugesan, P.; Anthony, D.M.G. Mathematical Analysis of Thermoregulation Effects on the Chemical reaction of Unsteady MHD BloodFlow through a Permeable Stretching Capillary with thermal radiation. *J. Porous Media* **2023**, *2023*, 167. [CrossRef]
4. Zain, N.M.; Ismail, Z. Numerical solution of magnetohydrodynamics effects on a generalised power law fluid model of blood flow through a bifurcated artery with an overlapping shaped stenosis. *PLoS ONE* **2023**, *18*, e0276576. [CrossRef] [PubMed]
5. Ashraf, M.U.; Qasim, M.; Shafie, S. Magnetohydrodynamic (MHD) peristaltic flow of blood containing cylindrical shaped gold nanoparticles in a non-uniform tube in the presence of Joule dissipation. *J. Magn. Magn. Mater.* **2023**, *578*, 170708. [CrossRef]
6. Zain, N.M.; Ismail, Z. Dynamic Response of Heat Transfer in Magnetohydrodynamic Blood Flow Through a Porous Bifurcated Artery with Overlapping Stenosis. *J. Adv. Res. Fluid Mech. Therm. Sci.* **2023**, *101*, 215–235. [CrossRef]
7. Afzal, S.; Qayyum, M.; Riaz, M.B.; Wojciechowski, A. Modeling and simulation of blood flow under the influence of radioactive materials having slip with MHD and nonlinear mixed convection. *Alex. Eng. J.* **2023**, *69*, 9–24. [CrossRef]
8. Alghamdi, W.; Alsubie, A.; Kumam, P.; Saeed, A.; Gul, T. MHD hybrid nanofluid flow comprising the medication through a blood artery. *Sci. Rep.* **2021**, *11*, 836. [CrossRef] [PubMed]
9. Dharmaiah, G.; Prasad, J.R.; Balamurugan, K.; Nurhidayat, I.; Fernandez-Gamiz, U.; Noeiaghdam, S. Performance of magnetic dipole contribution on ferromagnetic non-Newtonian radiative MHD blood flow: An application of biotechnology and medical sciences. *Heliyon* **2023**, *9*, e13369. [CrossRef]
10. Jiang, X.; Wang, J.; Wang, W.; Zhang, H. A Predictor–Corrector Compact Difference Scheme for a Nonlinear Fractional Differential Equation. *Fractal Fract.* **2023**, *7*, 521. [CrossRef]
11. Yang, X.; Wu, L.; Zhang, H. A space-time spectral order sinc-collocation method for the fourth-order nonlocal heat model arising in viscoelasticity. *Appl. Math. Comput.* **2023**, *457*, 192. [CrossRef]
12. Reddy, P.B.A.; Jakeer, S.; Basha, H.T.; Reddy, S.R.R.; Kumar, T.M. Multi-layer artificial neural network modeling of entropy generation on MHD stagnation point flow of Cross-nanofluid. *Waves Random Complex Media* **2022**, *2022*, 375. [CrossRef]

13. Rabbi, K.M.; Sheikholeslami, M.; Karim, A.; Shafee, A.; Li, Z.; Tlili, I. Prediction of MHD flow and entropy generation by Artificial Neural Network in square cavity with heater-sink for nanomaterial. *Phys. A Stat. Mech. Appl.* **2019**, *541*, 123520. [CrossRef]
14. Ullah, H.; Ullah, K.; Raja, M.A.Z.; Shoaib, M.; Nisar, K.S.; Islam, S.; Weera, W.; Al-Harbi, N. Numerical treatment of squeezed MHD Jeffrey fluid flow with Cattaneo Chrisstov heat flux in a rotating frame using Levnberg-Marquard method. *Alex. Eng. J.* **2023**, *66*, 1031–1050. [CrossRef]
15. Hajialigol, N.; Daghigh, R. The evaluation of the first and second laws of thermodynamics for the pulsating MHD nanofluid flow using CFD and machine learning approach. *J. Taiwan Inst. Chem. Eng.* **2023**, 782. [CrossRef]
16. Ali, F.; Awais, M.; Ali, A.; Vrinceanu, N.; Shah, Z.; Tirth, V. Intelligent computing with Levenberg–Marquardt artificial neural network for Carbon nanotubes-water between stretchable rotating disks. *Sci. Rep.* **2023**, *13*, 1–23. [CrossRef]
17. Kaswan, P.; Kumari, M. Analysis of a bioconvection flow of magnetocross nanofluid containing gyrotactic microorganisms with activation energy using an artificial neural network scheme. *Results Eng.* **2023**, *17*, 15. [CrossRef]
18. Kumar, R.S.V.; Sarris, I.; Sowmya, G.; Prasannakumara, B.C.; Verma, A. Artificial Neural Network Modeling for Predicting the Transient Thermal Distribution in a Stretching/Shrinking Longitudinal Fin. *J. Heat Transf.* **2023**, *145*, 1–46. [CrossRef]
19. Shilpa, B.; Leela, V.; Rani, H.P. Stability analysis of MHD radiative mixed convective flow in vertical cylindrical annulus: Thermal nonequilibrium approach. *Heat Transf.* **2022**, *52*, 707–733. [CrossRef]
20. Himika, T.A.; Hasan, F.; Molla, M.; Khan, A.I. LBM-MHD Data-Driven Approach to Predict Rayleigh–Bénard Convective Heat Transfer by Levenberg–Marquardt Algorithm. *Axioms* **2023**, *12*, 199. [CrossRef]
21. Shilpa, B.; Leela, V. LTNE effect on non-linear radiative MHD mixed convective flow in an annular porous medium: Intelligent Computing Paradigm. *Int. J. Ambient. Energy* **2023**, 1–16. [CrossRef]
22. Zhao, T.; Khan, M.I.; Chu, Y. Artificial neural networking (ANN) analysis for heat and entropy generation in flow of non-Newtonian fluid between two rotating disks. *Math. Methods Appl. Sci.* **2021**, *46*, 3012–3030. [CrossRef]
23. Nabwey, H.A.; Rashad, A.; Reddy, P.B.A.; Jakeer, S.; Mansour, M.; Salah, T. Radiative effects on unsteady MHD natural convection flow in an inclined wavy porous cavity using hybrid nanofluid containing a square obstacle. *Alex. Eng. J.* **2023**, *65*, 921–937. [CrossRef]
24. Jakeer, S.; Reddy, P.B.A. Entropy generation on the variable magnetic field and magnetohydrodynamic stagnation point flow of Eyring–Powell hybrid dusty nanofluid: Solar thermal application. *Proc. Inst. Mech. Eng. Part C J. Mech. Eng. Sci.* **2022**, *236*, 7442–7455. [CrossRef]
25. Jakeer, S.; Polu, B.A.R. Homotopy perturbation method solution of magneto-polymer nanofluid containing gyrotactic microorganisms over the permeable sheet with Cattaneo–Christov heat and mass flux model. *Proc. Inst. Mech. Eng. Part E J. Process. Mech. Eng.* **2021**, 993. [CrossRef]
26. Jakeer, S.; Reddy, S.; Rashad, A.; Rupa, M.L.; Manjula, C. Nonlinear analysis of Darcy-Forchheimer flow in EMHD ternary hybrid nanofluid (Cu-CNT-Ti/water) with radiation effect. *Forces Mech.* **2023**, *10*, 177. [CrossRef]
27. Waqas, H.; Farooq, U.; Yang, S.; Muhammad, T.; Imran, M. Heat transfer aspects in Carreau nanofluid having hybrid nanoparticles through a porous medium. *ZAMM Z. Angew. Math. Mech.* **2023**, *103*, 414. [CrossRef]
28. Wajihah, S.A.; Sankar, D.S. A review on non-Newtonian fluid models for multi-layered blood rheology in constricted arteries. *Arch. Appl. Mech.* **2023**, *93*, 1771–1796. [CrossRef]
29. Cherkaoui, I.; Bettaibi, S.; Barkaoui, A.; Kuznik, F. Numerical study of pulsatile thermal magnetohydrodynamic blood flow in an artery with aneurysm using lattice Boltzmann method (LBM). *Commun. Nonlinear Sci. Numer. Simul.* **2023**, *123*, 281. [CrossRef]
30. Faraz, F.; Siddique, I.; Imran, S.M.; Ali, B. Influence of multi-stratification and multi-slip on the radiative MHD flow of Carreau fluid. *Int. J. Mod. Phys. B* **2023**, 942. [CrossRef]
31. Algehyne, E.A.; Haq, I.; Rehman, S.; Raizah, Z.; Saeed, A.; Galal, A.M. Analysis of thermally stratified micropolar Carreau–Yasuda hybrid nanofluid flow with Cattaneo–Christov heat and mass flux. *J. Therm. Anal. Calorim.* **2023**, *148*, 5897–5916. [CrossRef]
32. Shojaei, S.; Shahgholi, M.; Karimipour, A. The effects of atomic percentage and size of Zinc nanoparticles, and atomic porosity on thermal and mechanical properties of reinforced calcium phosphate cement by molecular dynamics simulation. *J. Mech. Behav. Biomed. Mater.* **2023**, *141*, 105785. [CrossRef] [PubMed]
33. Koochaki, A.; Shahgholi, M.; Sajadi, S.M.; Babadi, E.; Inc, M. Investigation of the mechanical stability of polyethylene glycol hydrogel reinforced with cellulose nanofibrils for wound healing: Molecular dynamics simulation. *Eng. Anal. Bound. Elem.* **2023**, *151*, 55. [CrossRef]
34. Almitani, K.H.; Abu-Hamdeh, N.H.; Etedali, S.; Abdollahi, A.; Goldanlou, A.S.; Golmohammadzadeh, A. Effects of surfactant on thermal conductivity of aqueous silica nanofluids. *J. Mol. Liq.* **2020**, *327*, 114883. [CrossRef]
35. Lera, G.; Pinzolas, M. Neighborhood based Levenberg-Marquardt algorithm for neural network training. *IEEE Trans. Neural Netw.* **2002**, *13*, 1200–1203. [CrossRef]
36. Taheri, M.H.; Abbasi, M.; Jamei, M.K. Using artificial neural network for computing the development length of MHD channel flows. *Mech. Res. Commun.* **2019**, *99*, 8–14. [CrossRef]
37. Jakeer, S.; Reddy, P.B.A.; Basha, H.T.; Reddy, S.R.R. Entropy minimization of the non-Newtonian bio-hybrid (Fe_3O_4-CuO/blood) nanofluid flow over a linear extending sheet by means of induced magnetic field. *Int. J. Mod. Phys. B* **2023**, 142x. [CrossRef]
38. Basha, H.T.; Sivaraj, R. Numerical simulation of blood nanofluid flow over three different geometries by means of gyrotactic microorganisms: Applications to the flow in a circulatory system. *Proc. Inst. Mech. Eng. Part C J. Mech. Eng. Sci.* **2020**, *235*, 441–460. [CrossRef]

39. Basha, H.T.; Sivaraj, R.; Reddy, A.S.; Chamkha, A.J.; Tilioua, M. Impacts of temperature-dependent viscosity and variable Prandtl number on forced convective Falkner–Skan flow of Williamson nanofluid. *SN Appl. Sci.* **2020**, *2*, 163. [CrossRef]
40. Hayat, T.; Ullah, I.; Farooq, M.; Alsaedi, A. Analysis of non-linear radiative stagnation point flow of Carreau fluid with homogeneous-heterogeneous reactions. *Microsyst. Technol.* **2018**, *25*, 1243–1250. [CrossRef]
41. El-Dabe, N.T.; Ghaly, A.Y.; Rizkallah, R.R.; Ewis, K.M.; Al-Bareda, A.S. Numerical Solution of MHD Boundary Layer Flow of Non-Newtonian Casson Fluid on a Moving Wedge with Heat and Mass Transfer and Induced Magnetic Field. *J. Appl. Math. Phys.* **2015**, *3*, 649–663. [CrossRef]
42. Lin, H.-T.; Lin, L.-K. Similarity solutions for laminar forced convection heat transfer from wedges to fluids of any Prandtl number. *Int. J. Heat Mass Transf.* **1987**, *30*, 1111–1118. [CrossRef]